Pyrite iron isotope compositions track local sedimentation conditions through the Smithian-Spathian transition (Early Triassic, Utah, USA)

Marie-Noëlle Decraene, Johanna Marin-Carbonne, Christophe Thomazo, Arnaud Brayard, Anne-Sophie Bouvier, Brahimsamba Bomou, Thierry Adatte, Nicolas Olivier

Palaeogeography, Palaeoclimatology, Palaeoecology 617 (2023) 111507

Contents lists available at ScienceDirect

Palaeogeography, Palaeoclimatology, Palaeoecology

journal homepage: www.elsevier.com/locate/palaeo

Pyrite iron isotope compositions track local sedimentation conditions through the Smithian-Spathian transition (Early Triassic, Utah, USA)

Marie-Noëlle Decraene [a,*], Johanna Marin-Carbonne [a], Christophe Thomazo [b,c], Arnaud Brayard [b], Anne-Sophie Bouvier [a], Brahimsamba Bomou [a], Thierry Adatte [a], Nicolas Olivier [d]

[a] Institut des Sciences de la Terre, Université de Lausanne, Lausanne, Switzerland
[b] Biogéosciences, UMR6282, CNRS, Université Bourgogne, 6 Boulevard Gabriel, 21000 Dijon, France
[c] Institut Universitaire de, France
[d] Université Clermont Auvergne, CNRS, IRD, Laboratoire Magmas et Volcans, F-63000 Clermont-Ferrand, France

ARTICLE INFO

Editor: S Shen

Keywords:
Fe-isotope
Pyrite
Early Triassic
Smithian-Spathian transition
Utah

ABSTRACT

The late Smithian and the Smithian-Spathian boundary (SSB) are associated with harsh environmental conditions, including abrupt temperature changes, oceanic acidification and oxygen deficiency causing an additional marked loss of biotic diversity in the aftermath of the end-Permian mass extinction. Such environmental disturbances are documented worldwide through large fluctuations of the C, O, S and N biogeochemical cycles. This study presents secondary ion mass spectrometry pyrite Fe isotope analyses from the Lower Weber Canyon (LWC) section (Utah, USA) combined with bulk rock $\delta^{34}S_{py}$ and $\delta^{34}S_{CAS}$ analyses in order to better understand the redox changes in different environmental settings along a ramp depositional system through the SSB. $\delta^{56}Fe$ analyses show a large variability along the studied ramp system of ~7‰ (from −1.99 to +5.39‰), over a set of 350 microscale analyses. Bulk sulfide sulfur isotope analyses, performed on 30 samples, show $\delta^{34}S_{py}$ varying from −20.5 to +16.3‰. The inner ramp domain is characterized by a mean negative $\delta^{34}S_{py}$ values of −11.4‰. A progressive ^{34}S-enrichment (up to +16.3‰) is recorded in pyrite from mid and outer ramp settings. Carbonate associated sulfate (CAS) sulfur isotope analyses, performed on 5 samples, show relatively steady $\delta^{34}S_{cas}$ of +30.2 ± 2.2‰. Variations in $\delta^{34}S_{py}$ are interpreted as reflecting the degree of connection between sediment porewaters and the overlying water column. Multiple lines of evidence point to a fully oxygenated water column and thus restricts pyrite formation to the sediments. Both the sedimentary environment and the nature of deposits seem to control $\delta^{56}Fe_{py}$. In the inner ramp, high $\delta^{56}Fe_{py}$ values averaging +2.05‰ are only observed in microbially induced sedimentary structures (MISS), which record partial Fe-oxide reduction and oxidation reactions occurring at biofilms scale. In the absence of MISS, $\delta^{56}Fe_{py}$ inner ramp values are lighter ($\delta^{56}Fe_{mean}$ = +0.90‰) and reflect total reduction of Fe-oxides. In more distal and deeper mid and outer ramp settings, Fe isotope compositions are controlled by microbially-produced H_2S that scavenged iron into sulfides. This study unravels local redox state changes in the upper part of some marine sediments by coupling Fe and S isotope systematics. It demonstrates that pyrite grains, and their sulfur and iron isotopic compositions, formed throughout the SSB should be used with caution to infer the redox state of the ocean after the Permian-Triassic biotic crisis.

1. Introduction

Only ~2 Myr after the devastating end-Permian mass extinction (~252 Ma), the ocean-atmosphere system underwent successive and abrupt environmental and biotic changes at the Smithian-Spathian Boundary (SSB; e.g. Galfetti et al., 2007). Significant disturbances of the global carbon, sulfur, oxygen, and nitrogen biogeochemical cycles underline sustained environmental stresses. These include climate warming up to the beginning of the late Smithian, followed by a rapid cooling across the latest Smithian and the SSB (Goudemand et al., 2019;

Abbreviations: Smithian/Spathian Boundary, SSB; Secondary Ion Mass Spectrometer, SIMS; Scanning Electron Microscope, SEM; Microbial Sulfate Reduction, MSR; Dissimilatory Iron Reduction, DIR.

* Corresponding author.
E-mail address: marie-noelle.decraene@unil.ch (M.-N. Decraene).

https://doi.org/10.1016/j.palaeo.2023.111507
Received 11 November 2022; Received in revised form 3 March 2023; Accepted 9 March 2023
Available online 14 March 2023

Zhang et al., 2019), the spread of anoxia through ocean stratification (Song et al., 2019) or development of oxygen minimum zones (Algeo et al., 2011), and ocean acidification potentially linked with greenhouse gases released by large igneous province eruption (Grasby et al., 2013; Zhao et al., 2020). All combined, these deleterious conditions led to a marked loss in ecosystem diversity and a severe extinction of several nekton-pelagic organisms during the late Smithian (Brayard et al., 2006; Orchard, 2007; Jattiot et al., 2016). Several proxies such as sulfate and sulfide $\delta^{34}S$ values, paired carbonate and organic matter $\delta^{13}C$ values, Ce anomalies, trace elements (e.g. Mn, V, U, Mo, Mo/Al ratio), iron speciation and size of framboidal pyrite suggest occurrences of transient anoxia in the water column that could have spread onto continental shelves (Grasby et al., 2013; Song et al., 2013; Zhang et al., 2015; Elrick et al., 2017; Song et al., 2019; Zhang et al., 2019). Although anoxic and/or euxinic conditions seem to be recurrent in the Early Triassic deep ocean, well-oxygenated shallow-marine environments, as well as diversified and complex ecosystems are also documented (Beatty et al., 2008; Hautmann et al., 2011; Collin et al., 2015; Brayard et al., 2017; Olivier et al., 2018; Smith et al., 2021; Dai et al., 2023). Reconstructing the redox state of the water column together with the sediment porewaters is therefore key to better understand the evolution of the environmental conditions in space and time that prevailed through the late Smithian and the SSB, and that may have markedly influenced the biotic recovery in the aftermath of the end-Permian mass extinction.

As a mineral made of redox-sensitive elements, pyrite (FeS_2) is used to infer the oxygenation state of the ocean through the study of its morphology, size, trace element content and isotope (S and/or Fe) compositions (Wilkin et al., 1996; Wilkin and Barnes, 1997; Shen et al., 2003; Bond and Wignall, 2010; Gregory et al., 2015). Oxidation of Fe(II) into Fe(III) is associated with a large equilibrium fractionation producing ^{56}Fe-depleted dissolved Fe(II) (Welch et al., 2003), which can be later recorded in Fe-bearing minerals such as pyrite. Large ^{56}Fe-depletion during redox processes is however only expressed for the partial reaction of the dissolved iron reservoir, i.e., during partial oxidation of aqueous Fe^{2+} (Rouxel et al., 2005). Consequently, assuming that redox reaction occurred through Earth history and that $\delta^{56}Fe$ values reflect primary processes, secular variations of Fe isotope compositions can be interpreted in terms of global oxygenation state changes (Rouxel et al., 2005). Other studies propose that low $\delta^{56}Fe$ values reflect transport of microbially reduced dissolved Fe(II) from the shelf to the basin along the chemocline (Johnson and Beard, 2005; Severmann et al., 2008). Alternatively, another scenario, which does not require Fe redox cycling, suggests that $\delta^{56}Fe$ values reflect primarily the rate of pyrite precipitation (kinetic or equilibrium) that is highly dependent on the sulfur availability (Guilbaud et al., 2011; Mansor and Fantle, 2019). Therefore, the interpretation of pyrite iron isotope compositions in terms of water oxygenation state can be obscured by the involvement of redox and non-redox processes, inheritance of isotopic fractionation of the Fe source, size of the sulfide reservoir, and early diagenetic processes (Severmann et al., 2008; Virtasalo et al., 2013; Busigny et al., 2014; Marin-Carbonne et al., 2020). Further, on a more local scale, processes occurring within the upper part of the sedimentary column (from the upper centimeters to meter depth), can produce Fe isotope variations up to 5‰. Such variations are partially to entirely decoupled from global biogeochemical cycling in the water column, resulting in the isotopic evolution of Fe(II) or Fe-oxide reservoirs in the sediments (Archer and Vance, 2006; Virtasalo et al., 2013; Lin et al., 2017). Some ambiguities in the interpretation of the pyrite $\delta^{56}Fe$ can be lessened by pairing this measurement with the $\delta^{34}S$ signal. For instance, positive covariation between pyrite $\delta^{56}Fe$ and $\delta^{34}S$ signals through Archean-Paleoproterozoic transition suggests an expansion of the sulfidic Fe sink (Heard and Dauphas, 2020). Such positive covariations have also been evidenced in 2.7 Ga sedimentary pyrite from the Belingwe greenstone belt and interpreted as early diagenetic signatures of coexisting microbial Fe and S reduction (Archer and Vance, 2006).

The aim of this study is to distinguish in the context of the Smithian-Spathian transition whether pyrite paired Fe—S isotopic signatures (1) record redox condition variations of the seawater, (2) reflect variations of the Fe/S ratio or (3) are controlled by early diagenesis and/or microbial processes within the sediments or at the seawater/sediment interface. For this purpose, we present spatially resolved $\delta^{56}Fe$ associated with chemostratigraphic $\delta^{34}S$ records along the Lower Weber Canyon sedimentary succession (Fig. 1a; Utah, USA), which is characterized by various sedimentary rocks deposited between shallow inner to deeper outer ramp settings. The combination of petrological observations, in situ $\delta^{56}Fe_{py}$ analyses by SIMS, bulk rock $\delta^{34}S$ analyses and total organic carbon concentrations allowed us to unravel pyrite formation pathways within the sediments from different facies.

2. Materials and methods

2.1. Geological context, studied section and samples

During the Permian-Triassic interval, the near equatorial region of western Pangea was an active tectonic compression zone, leading to the formation of the Sonoma orogeny and the associated Sonoma Foreland Basin (SFB; Fig. 1; Burchfiel and Davis, 1975; Ingersoll, 2008; Dickinson, 2013). Lower Triassic sedimentary rocks of the SFB mainly cover present-day eastern Idaho, eastern Nevada and Utah (USA; Caravaca et al., 2018). The Early Triassic sea-level rise resulted in a sedimentary succession exhibiting continental terrigenous conglomerates and sandstones of the Moenkopi Group on the south and eastern sides of the basin, interfingering with marine carbonates of the Thaynes Group towards the north and western sides (Paull and Paull, 1993; Lucas et al., 2007; Brayard et al., 2013). In the SFB, a transgression that corresponds to the second 3rd order T-R (transgressive-regressive) sequence of the Smithian is recorded (Haq et al., 1987; Embry, 1997), which was controlled by regional tectonics and climate (Olivier et al., 2014; Caravaca et al., 2018; Brayard et al., 2020). Calibrations of late Smithian to early Spathian sedimentary sections within the basin are based on ammonoid biostratigraphy (Guex et al., 2010; Brayard et al., 2013, 2021). The late Smithian *Anasibirites* beds represent the maximum flooding at the scale of the basin (Brayard et al., 2013, 2020). The SFB is also characterized by occurrence of morphologically various, mineralized or not, microbial deposits, mainly in the southern part of the SFB (Schubert and Bottjer, 1992; Pruss et al., 2004; Brayard et al., 2011; Olivier et al., 2014, 2016, 2018; Woods, 2014; Vennin et al., 2015; Grosjean et al., 2018; Kirton and Woods, 2021). The studied sedimentary section (described below) includes Smithian microbially deposits characterized by microbially induced sedimentary structures (MISS; see Grosjean et al., 2018).

This study focuses on the Lower Weber Canyon (LWC) section, for which petrographic descriptions and interpretation in terms of depositional environments are detailed in Grosjean et al. (2018). According to these authors, the LWC section can be divided in four lithologic units (A-D). This study concentrates on the two units (B and C) preceding and including the SSB (Fig. 1). Unit B is 111 m thick and mainly made of carbonated siltstones, including organic-rich laminae recognized as MISS, and few levels of bioclastic calcarenites. Siltstone-rich sediments of the Unit B reflect a peritidal depositional environment in an inner ramp system. Sediments of this unit are of middle Smithian age as they belong to the *Meekoceras* ammonoid assemblage (Grosjean et al., 2018; Brayard et al., 2021). The 36 m-thick Unit C consists of silty mudstones that are intercalated with bioclastic limestones. The lower part of this unit includes the late Smithian *Anasibirites* ammonoid assemblage (Brayard et al., 2021) and the SSB. The mudstone-rich deposits of the Unit C reflect a mid to outer ramp setting that occasionally recorded storm events. Eight rock samples were collected in the Units B and C, thus representing different depositional environments distributed along an inner to outer ramp system (Fig. 1). Their deposition during the SSB, the diversity of depositional environments (from peritidal siltstones to deeper outer ramp mudstones), and associated facies including

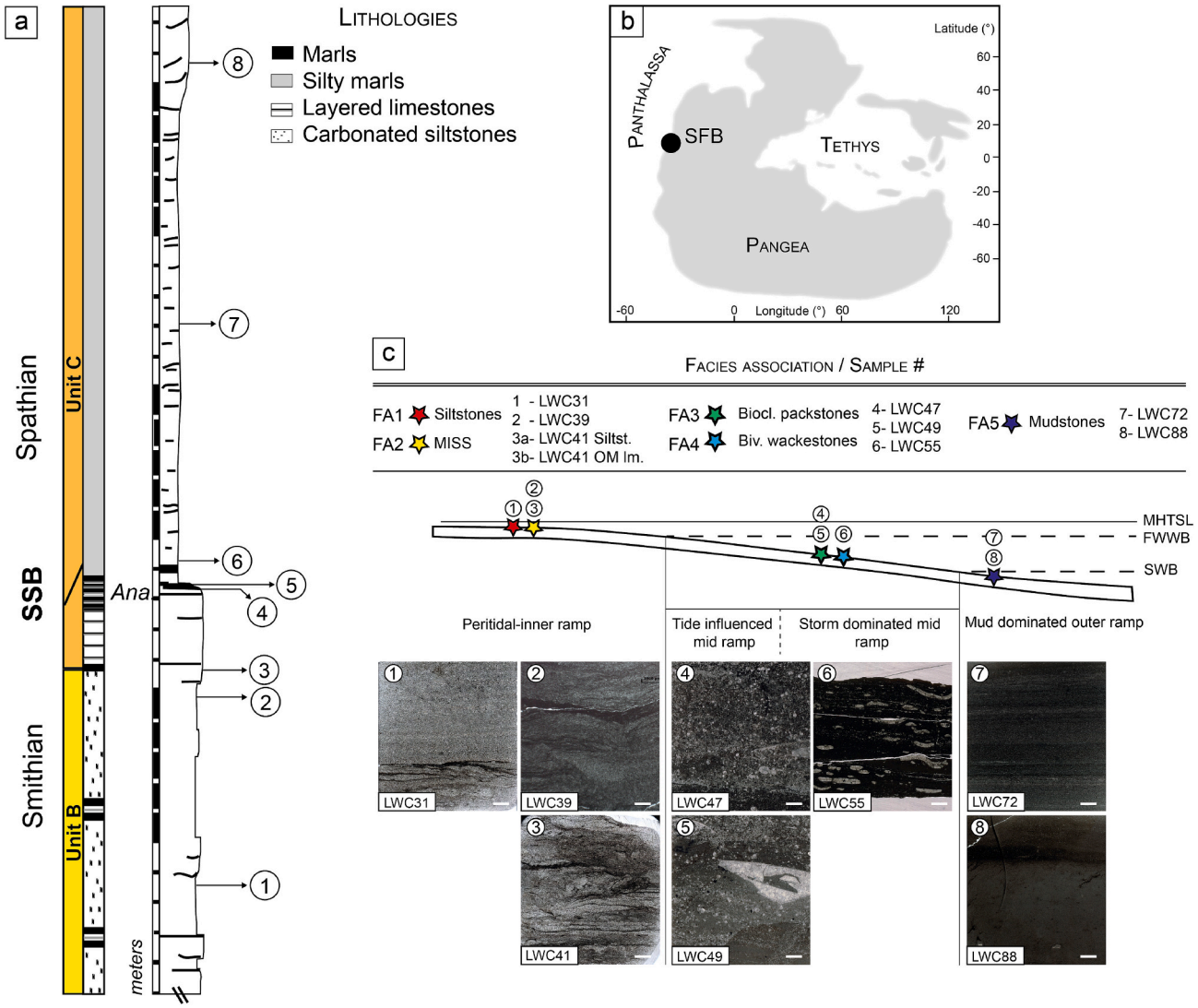

Fig. 1. a) Log of the LWC section with focus on Units B and C (modified after Grosjean et al., 2018). b) Early Triassic paleogeographic map showing the location of the Sonoma Foreland Basin (SFB; modified after Brayard et al., 2013). c) Position along a ramp system and thin section pictures of studied samples (scale bar for thin sections: 2.5 mm). The different star colors refer to the corresponding facies association (FA1-FA5). MHTSL: Mean High Tide Sea Level; FWWB: Fair Weather Wave Base; SWB: Storm Wave Base.

occurrences of MISS in a shallow and proximal environment, are relevant parameters to decipher controlling parameters on Fe isotope signatures of pyrite. A description of facies associations and corresponding depositional environments is detailed in the section 3.1.

2.2. Methods

2.2.1. Petrographic observations

Petrographic descriptions were carried out on polished thick sections using a Scanning Electron Microscope (SEM) at ISTE Lausanne (Tescan Mira LMU). Backscattered electron images were performed at a working distance of 21 mm using a voltage of 20 kV and a current of 1.5 nA. Semi quantitative spot analyses were done by energy dispersive X-ray spectrometry to determine elemental composition of the sulfides. Bulk rock mineralogical analyses were conducted at the Institute of Earth Sciences of the University of Lausanne, Switzerland (Thermo Scientific ARL X-TRA Diffractometer) using the procedure described by Klug and Alexander (1974) and Adatte et al. (1996). These analyses were performed on powdered samples pressed into powder holders. This method for semi-quantitative analysis of the bulk rock mineralogy used external standards with elemental compositions based on mineral stoichiometries. The error varies between 5 and 10% for the phyllosilicates and 5% for grain minerals. The non-quantified portion corresponds generally to poorly crystallized iron hydroxides, phyllosilicates, and nearly amorphous material. This portion represents here less than 2% of the bulk composition.

The chemical composition of pyrite was investigated by Electron Probe Micro-Analyzer (EPMA) using a JEOL JXA-8530F at ISTE Lausanne in order to quantify the trace content of zoning pyrite. The acceleration voltage was 15 kV and beam current was 15 nA focused in 3 μm. Reference materials, including sulfides, oxides, and silicates, were tested before the analysis of S, Fe, Co, Mn, Pb, Ti, Cr, Zn, Cu and Ni. Detection limits were 133 ppm for S, 130 ppm for Fe, 141 ppm for Co, 129 ppm for Mn, 327 ppm for Pb, 79 ppm for Ti, 145 ppm for Cr, 238 ppm for Zn, 199 ppm for Cu and 150 ppm for Ni.

Carbonaceous matter has been characterized by Raman spectroscopy. Raman data were obtained using a Horiba Jobin Yvon LabRAM HR800 spectrometer (ISTE, UNIL) in a confocal configuration equipped with an Ar^{+} 532 nm laser and a CCD detector. Measurements were performed at room temperature on thin sections, with a laser power delivered at the sample surface <1 mW to prevent thermal damage. This technique allows to document the structural organization of the

aromatic skeleton of carbonaceous matter, and to estimate the peak metamorphic temperature experienced by the carbonaceous matter (Beyssac et al., 2002). Peak temperature estimations were done following the methodology proposed by Kouketsu et al. (2014).

2.2.2. Hg concentrations, TOC contents and trace elements

Mercury concentrations were measured using a Zeeman R-915F (Lumex, Saint-Petersburg, Russia) high-frequency atomic absorption spectrometer at the University of Lausanne. Hg was extracted by thermal evaporation at 700 °C from solid samples that were previously powdered. Analyses were bracketed by the measurement of a certified external standard (GSD-11, Chinese alluvium, Hg concentration: 72 ± 6 ppb) and two aliquots were systematically analyzed. To be exempt of biased Hg peaks due to affinity of Hg with organic carbon and sulfide, measured Hg concentrations were normalized to TOC and sulfur concentrations.

Total organic carbon (TOC in wt%) contents were obtained through Rock-Eval 6 analyses at University of Lausanne following the procedure of Espitalié et al. (1985) and Behar et al. (2001). The reference material IFP 160000 (French Institute of Petroleum) was used to calibrate the measurements and the precision was <0.1%. Analyses consist of a combined pyrolysis of ~60 mg of powdered samples followed by oxidation of the residue.

The analyses of Trace element concentrations were performed by Inductively Coupled Plasma Mass Spectrometry (ICP-MS) at the Activation Laboratory (Actlabs) in Ancaster, Canada. The method used is Lithium Metaborate/Tetraborate Fusion ICP and ICP-MS. Reproducibility was checked by seven duplicate and replicate analyses of laboratory standards and is better than 2% (1σ) for major and trace elements.

2.2.3. Bulk rock $\delta^{34}S$ analyses

Sulfide sulfur was retrieved using a conventional wet chemical extraction at the Biogéosciences Laboratory, Dijon, France. Acid volatile sulfide (AVS), representing monosulfides, and chromium reducible sulfur (CRS) consisting primarily of pyrite were extracted sequentially. First, AVS was liberated using cold concentrated HCl for 2 h. If any, resulting hydrogen sulfide was precipitated as Ag_2S with a 0.3 M $AgNO_3$ solution. Subsequently, CRS was released using a hot and acidic 1.0 M $CrCl_2$ solution following the method described in Gröger et al. (2009). The resulting H_2S was precipitated as Ag_2S. After centrifugation, the silver sulfide precipitate was washed several times with deionized distilled water and dried at 50 °C for 48 h in an oven and weighted. Mass balance was used to calculate the amount of AVS and CRS. Concentrations in ppm are reported individually in Table S1 (note that AVS were below the detection limit in all samples).

CAS sulfur was retrieved using a wet chemical extraction. Fifty grams of carbonate samples (with carbonate contents typically >70 wt% of the total rock) were powdered, soluble sulfates being leached by a 1.7 M NaCl solution for 4 h, followed by four rinses in deionized water. This step was repeated five times and the powder was then dissolved in 4 N HCl (12*h*). The acidified samples were then filtered, on a 0.45 μm nitrocellulose paper and an excess of 250 $g.l^{-1}$ of $BaCl_2$ solution was added to the filtrate to precipitate $BaSO_4$. After centrifugation, the barium sulfate precipitate was washed several times with deionized distilled water and dried at 60 °C for 24 h in an oven.

The $\delta^{34}S$ measurements were performed at the Biogéosciences Laboratory, Dijon, France, on SO_2 molecules via combustion of ~500 μg of samples (silver sulfide and barium sulfate) homogeneously mixed with an equal amount of tungsten trioxide using a Vario PYRO cube (Elementar GmbH) connected online via an open split device to an IsoPrime isotope ratio mass spectrometry (IRMS) system (Isoprime, Manchester, UK). International standards IAEA-S-1, IAEA-S-2, IAEA-S-3 and NBS-127 were used for calibration assuming $\delta^{34}S$ values of −0.3‰, +22.7‰, −32.3‰ and 20.3‰ (VCDT), respectively. Analytical reproducibility was better than ±0.4‰ (1σ) based on replicates for standard materials and samples.

2.2.4. Fe isotope analyses by SIMS

Iron isotope compositions were measured over four SIMS sessions (March 2020, June 2020, November 2020, September 2021) using the Cameca ims 1280 HR2 at the SwissSIMS (University of Lausanne). Iron isotope compositions are expressed in delta notation, reporting permil variations of the $^{56}Fe/^{54}Fe$ ratios normalized to IRMM-014 as the following:

$$\delta^{56}Fe = \left[\frac{\left(\frac{^{56}Fe}{^{54}Fe}\right)_{sample}}{\left(\frac{^{56}Fe}{^{54}Fe}\right)_{IRMM014}} - 1 \right] * 1000$$

In order to preserve high vacuum conditions of $\sim 10^{-9}$ mbar in the analytical chamber and avoid hydride formations, thick sections were polished and pressed into one-inch indium mounts. Balmat pyrite standard was used over the sessions to assess the stability of the instrument ($\delta^{56}Fe = -0.40 \pm 0.01$‰; Marin-Carbonne et al., 2011) and was included in each sample mount. The conductivity of the sample surface was ensured by a 35 nm-thick gold coating. A total of 350 analyses of pyrite was performed in 8 different samples following the method described in Decraene et al. (2021). Briefly, a 10 kV, 3 nA Gaussian $^{16}O^-$ primary beam was focused into a 2.5 to 3 μm spot. $^{52}Cr^+$, $^{54}Fe^+$, $^{56}Fe^+$ and $^{57}Fe^+$ secondary ions were collected simultaneously by electron multipliers (L2 for $^{52}Cr^+$) and off-set faraday cups (C for $^{54}Fe^+$, H1 for $^{56}Fe^+$ and H′2 for $^{57}Fe^+$). We used an entrance slit width of 61 μm and the slit 3 of the multicollection to obtain a Mass Resolving Power at ~7000 (interference of ^{53}CrH on ^{54}Fe). The field aperture was set at 2000 μm and the energy slit at 50 eV. A 90 s presputtering time was applied to remove the surface contamination, followed by secondary ion beam centering and background detector measurements. Then, data acquisition is conducted for 300 s. Typical count rate for $^{56}Fe^+$ on Balmat standard was 4.50E+7 counts per second (cps) and the mean reproducibility was ±0.21‰ (2SD; Table S2). Instrumental mass fractionation (IMF) was corrected by standard bracketing. Iron isotope compositions are represented in the form of histogram or box plot. Histograms have been set with a bin size of 0.4‰, to both limit the production of artificial secondary peaks and bin boundary effects, and in a range of −2 to +6‰. The Shapiro-Wilk test was used to test whether the data are normally distributed (Table S3). In the case of Gaussian distributions, the parametric Student's *t*-test was employed to test the hypothesis of equal means for two independent samples. In the case of non-Gaussian distributions, the non-parametric Mann-Whitney test (two sided) was used to test the hypothesis of equal medians for two independent samples. Both tests gave results as *p*-values with a confidence interval of 95% (Tables S4-S7).

3. Results

3.1. Facies description

According to Grosjean et al. (2018), the eight studied samples belong to five different facies associations. These facies are distributed along a ramp depositional profile from proximal and shallow siliciclastic dominated deposits to more distal and deeper mud-dominated sediments (Fig. 1). The bulk mineralogical composition of all samples is predominantly composed of calcite, quartz, phyllosilicates, and plagioclase.

The inner peritidal ramp setting is dominated by two facies associations, termed carbonated-siltstones (FA1) and organic-rich laminae (FA2). It should be noted that LWC41 encloses these two facies FA1 and FA2, named respectively LWC41 Siltst. and LWC41 OM, in which pyrite is observed. FA1 consists of calcite, quartz, phyllosilicates, and dolomite (see supplementary materials; Fig. S1). Small fragmented bioclasts are observed as well as accessory minerals such as apatite, zircon and anatase. This facies association corresponds to samples LWC41 Siltst.

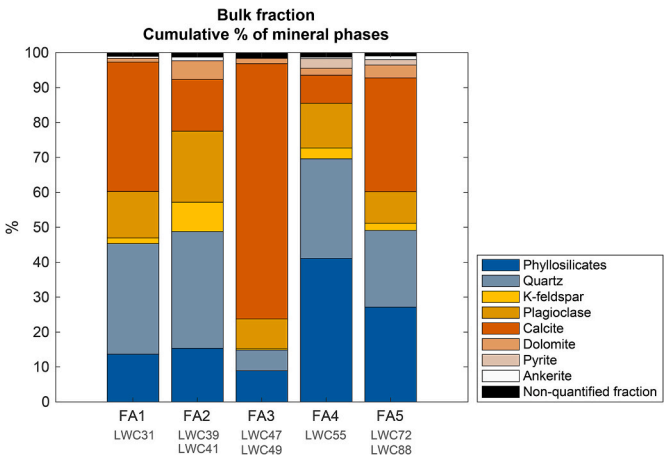

Fig. 2. Bulk mineralogical composition of the 8 LWC samples classified as a function of their facies.

and LWC31. FA2 is composed of undulated organic-matter laminae that are laterally discontinuous and locally reworked in a carbonated and silty matrix. These organic laminae and chips are interpreted by Grosjean et al. (2018) as MISS. Samples LWC39 and LWC41 OM are attributed to FA2. For mineralogical analyze purposes, LWC41 was not divided into two parts to distinguish FA1 and FA2. The bulk composition of LWC41 being similar to that of LWC39, LWC41 is processed here as only a part of FA2. The bulk mineralogical composition of LWC31 (Fig. 2) is dominated by calcite (37%) and quartz (32%). The phyllosilicate content is up to 14% and is similar to the plagioclase content (13%). K-feldspars are present in small proportion (2%), as well as dolomite and ankerite, which contents are below 1%. The average bulk composition of FA2 is dominated by quartz (33%), plagioclase (20%), phyllosilicates (15%) and calcite (15%; Fig. 2). The proportion of carbonates is much lower than that of FA1. The dolomite content is higher than in FA1 (5%) whereas the ankerite content is still low (1%; Fig. 2).

Samples from the mid ramp setting reflect two facies associations, termed bioclastic packstones (FA3; LWC47 and LWC49) and bioclastic wackestones (FA4; LWC55). FA3 consists of calcite, phyllosilicates and quartz (Fig. S1). Few apatites and oxides are also observed. Bivalve and ammonoid shells are recrystallized by sparite. The average bulk mineralogical composition of samples from FA3 shows a dominance of calcite (73%) relative to the other phases (Fig. 2). Phyllosilicates and quartz represent 9 and 6% of the bulk composition. The amount of K-feldspar is low (below 1%) whereas the amount plagioclase is up to 9%. The sum of the dolomite and ankerite content is below 2% (Fig. 2). FA4 is made of sparite-filled bivalves following a planar distribution in a calcite dominated matrix with common small quartz grains. Apatite and zircon grains are present as accessory minerals. The mineralogy of LWC55 (Fig. 2) is dominated by phyllosilicates (41%) and quartz (29%). This sample contains 13% of plagioclase and 8% of calcite. The amount of K-feldspar and dolomite are of 3% and 2% respectively. The ankerite content is below 1%. Pyrite was detected in a small proportion of 3%.

Samples from the mud-dominated outer ramp correspond to a mudstone facies association (FA5; LWC72 and LWC88). These sediments deposited closed to the mid to outer ramp transition as they consist of mudstone sometimes interbedded with rare thin layers made of small quartz grains. Apatite, zircon, anatase and chalcopyrite are present as accessory mineral phases. The bulk mineralogical composition of samples from FA5 (Fig. 2) contains up to 33% of calcite, 27% of phyllosilicates and 22% of quartz. The plagioclase and K-feldspar contents are respectively of 9 and 2%. The respective amount of dolomite and ankerite are of 4% and 1%. Finally, pyrite is present in a smaller proportion than in FA4, representing 2% of the bulk composition.

3.2. Carbon, sulfur and trace element contents

Total organic contents vary from 0.04 to 0.49 wt% and show an enrichment across the SSB, with a maximum TOC content recorded in LWC55 (Fig. 3). TOC concentrations for samples LWC39 and LWC41 are biased due to the heterogeneous distribution of organic-rich laminae in the analyzed samples. Sulfur content of 30 LWC samples (from LWC31 to LWC70) vary between 21 and 12,357 ppm with a mean value of 2585 ppm (Fig. 3 and Table S1). Sulfur content is highly variable with highest concentrations recorded in samples deposited during and immediately after the SSB. Inner ramp samples (LWC31 to LWC42) show S concentrations between 21 and 3780 ppm, with an average of 1222 ppm (Table S1). There is no difference in sulfide content between samples from siltstone facies (FA1) and MISS facies (FA2). Sulfur concentrations in samples from mid ramp setting range from 296 to 11,472 ppm and show the highest average value (4232 ppm). Samples from the outer ramp system exhibit the larger variation, from 61 to 12,358 ppm. The Sr and Mn contents have also been measured in these 30 samples (LWC31 to LWC70; Table S1). The Sr content varies from 17 to 284 ppm, with an average value of 105 ppm. The Mn content varies between 264 ppm and 6900 ppm, with an average value of 2308 ppm. These 30 samples show an average Mn/Sr ratio of 24, with a range of variation between 11 and 40. Mercury concentrations vary between 2.70 and 25.55 ppb (Table S8, Fig. S2). Normalization with TOC and S contents does not show any Hg enrichment in the studied samples.

3.3. Bulk pyrite and CAS $\delta^{34}S$ values

The $\delta^{34}S_{py}$ values show a large range of variations from −20.5 to +16.3‰ (Fig. 3, Table S1). Except for three samples, only negative $\delta^{34}S$ values are recorded in the inner and the mid ramp systems, while the majority of $\delta^{34}S$ values in the outer ramp are positive. The inner ramp setting shows highly variable $\delta^{34}S$ values, ranging from −20.5 to +5.8‰, with an average value of −11.4 ± 9.3‰ (1SD). The mid ramp setting documents small variations with a $\delta^{34}S$ average of −4.0 ± 4.0‰ (1SD). The outer ramp system displays the highest S isotope compositions, ranging from −7.3 to +16.3‰, and an average value of +6.4 ± 7.4‰ (1SD). The $\delta^{34}S$ signal of sedimentary sulfide shows a ^{34}S enrichment tendency from the base to the top of the LWC section. The $\delta^{34}S_{CAS}$ signal measured on five samples across the section does not exhibit noticeable secular variations (Fig. 3; Table S1). Indeed, $\delta^{34}S_{CAS}$ values range from 29.2 to 33.5‰, with a mean value of 30.2 ± 2.2‰ (1SD).

3.4. Pyrite description

In the eight studied samples, pyrite grains display various morphologies, categorized as euhedral, framboid, aggregated and framboid with secondary overgrowth. Their size ranges between 5 and ~ 100 μm (Fig. S3). Only LWC31 displays a large pyrite nodule of ~3 mm wide. Pyrite with a size of 5 to 40 μm tends to record a wider range of Fe isotopic compositions than pyrite larger than 40 μm (Fig. S3). However, it should be noted that a sampling bias may have been introduced by measuring a larger amount of pyrite 10–20 μm in size relative to pyrite larger than 30 μm.

Framboids are of particular interest as they are extensively studied to reconstruct paleoredox conditions and to constrain the locus of pyrite precipitation (Wilkin et al., 1996). In this study, the size of framboids ranges from 5 to 25 μm with an average size of 11 μm ($n = 43$; Fig. 4a). Moreover, the size distribution of framboids is monomodal, with a mode at around 10 μm, and highlights that most of the pyrite grains have a size between 5 and 12 μm (Fig. 4a). The absence of correlation between the grain size and their Fe isotope compositions (Fig. 4b) does not allow to define several generations of framboidal grains. The number of analyzed pyrite per morphology and facies and their corresponding Fe isotope compositions is detailed in section 3.6. Several remarkable pyrite

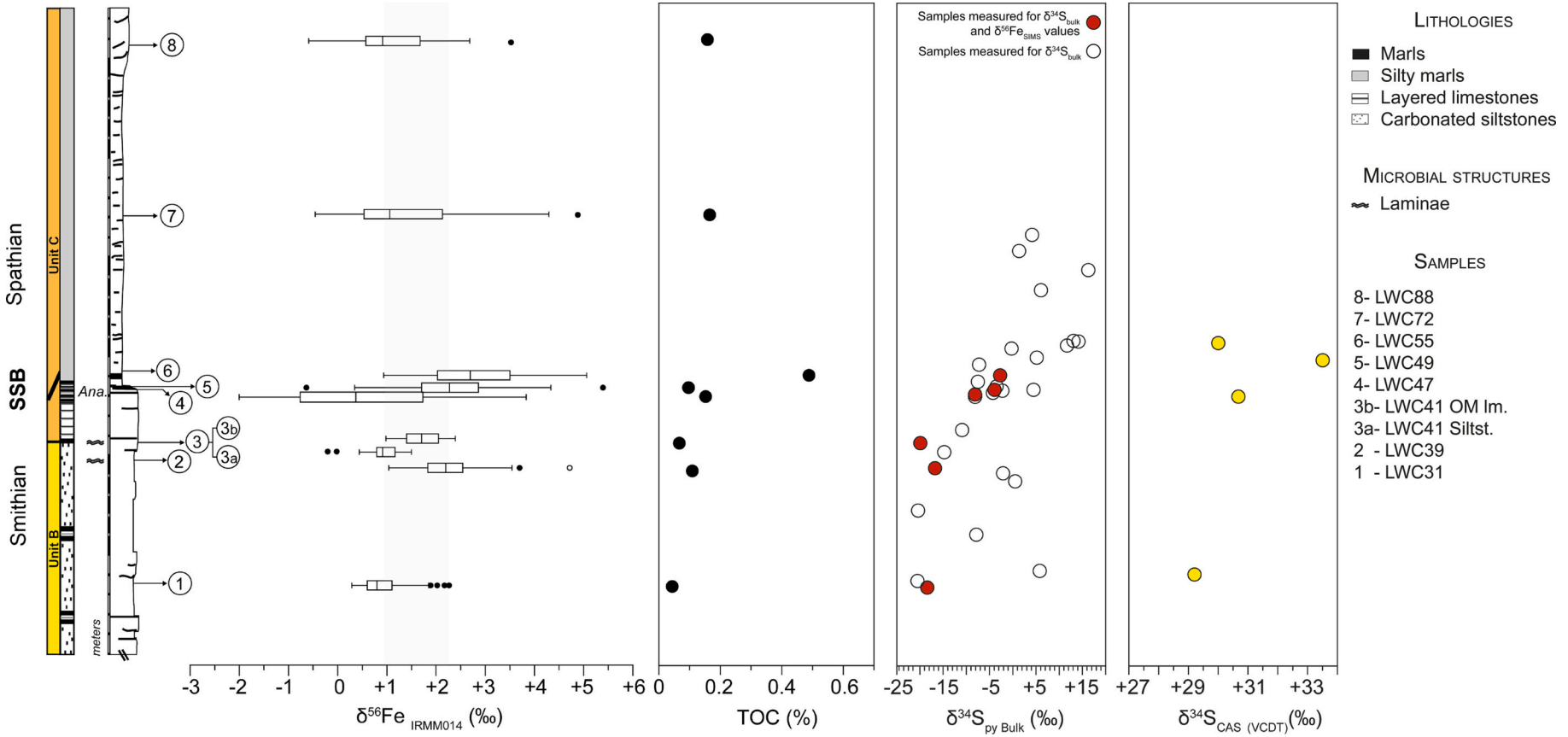

Fig. 3. Evolution of Fe isotope compositions measured by SIMS on 8 LWC samples with corresponding total organic carbon concentrations (in %), pyrite $\delta^{34}S$ values on 30 samples (LWC31 to LWC70) and carbonate associated sulfate (CAS) $\delta^{34}S$ values on 5 samples of the section. The simplified log reports lithologies and positions of samples measured by SIMS.

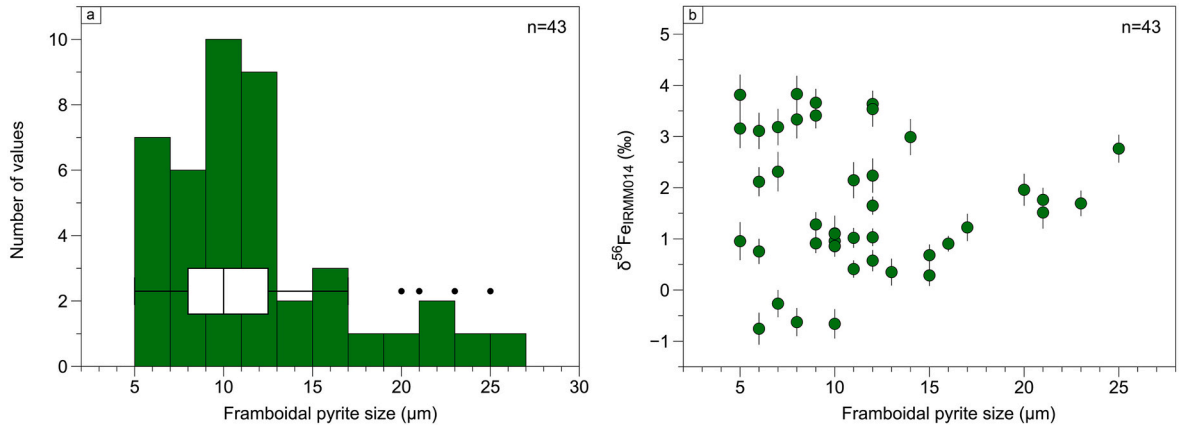

Fig. 4. a) Framboid size distribution (histogram and box plot) of the 43 framboids measured in five LWC samples (LWC47 to LWC88) and b) relationship between the size of framboid pyrite grains and their Fe isotope compositions.

features have been observed in the samples of the LWC section. In sample LWC41 (Siltst. and OM parts), pyrite is affected by secondary rims but still preserves framboidal cores (Fig. 5a). The nodule observed in LWC31 is made of an aggregate of euhedral pyrite grains whose former boundaries are still discernible at the nodule edge (Fig. 5b). Sample LWC49 encloses aggregated pyrite with chemical zoning enriched in Ni (Fig. 5c). These Ni enrichments have been evidenced through electronic microprobe analyses but, due to the size of the grains and the spatial resolution of electron beam, Ni concentrations were not quantified. A close association between pyrite and organic matter is shown in samples LWC31, LWC39, LWC41 and LWC88 (Fig. 5d). All Raman spectra obtained on these laminae show characteristics of poorly ordered carbonaceous material (Fig. S4), corresponding to maximum temperature of 150 °C consistent with burial diagenesis (Heydari and Moore, 1989).

3.5. *In situ iron isotope compositions*

Large variations of pyrite δ^{56}Fe values, from −1.99 to +5.39‰, are evidenced over 350 analyses through the studied section (Fig. 3; Table S9). In the inner ramp deposits (FA1 and FA2), 143 pyrite analyses show δ^{56}Fe values ranging from −0.21 to +4.72‰, and an average $\delta^{56}Fe_{py}$

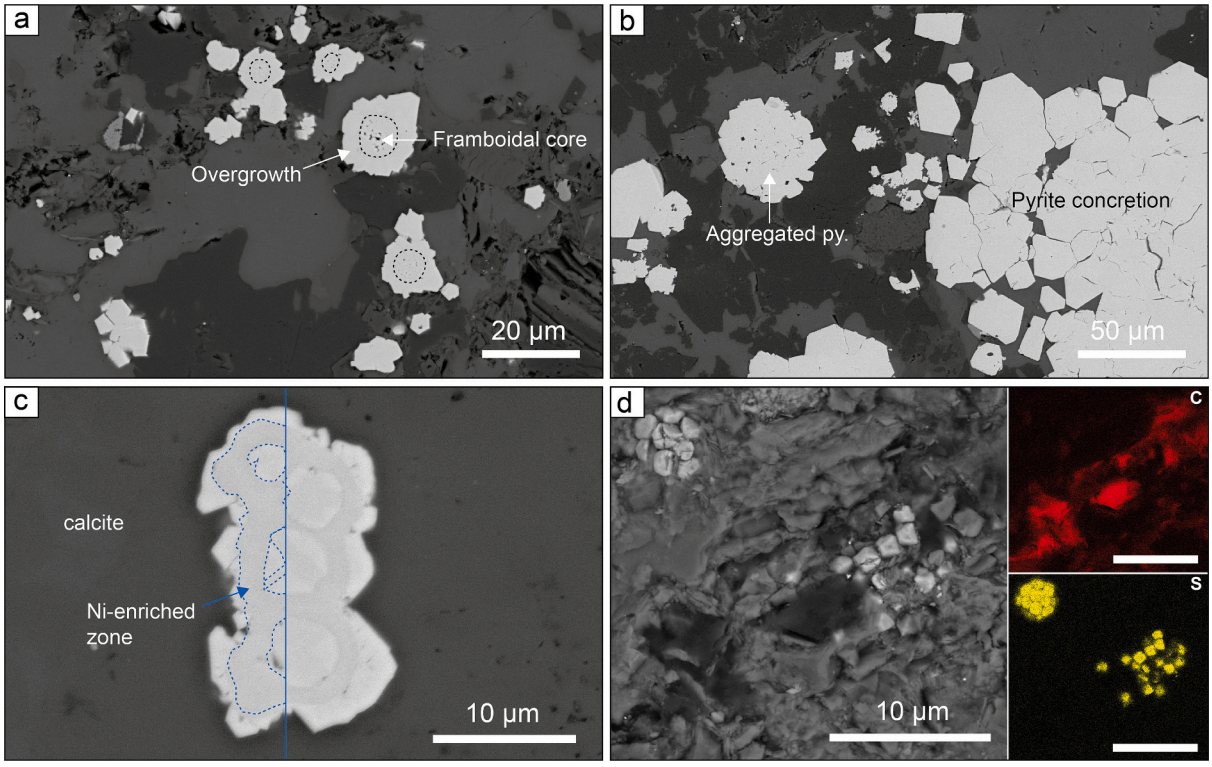

Fig. 5. Backscattered images of early diagenetic pyrite observed in LWC samples. Examples of a) framboids with overgrowths from LWC41 Siltst., b) aggregated grains and edge of the pyrite nodule observed in LWC31, c) a zoned (Ni-enriched) aggregate from LWC49. The Ni-enrichment was evidenced by electronic microprobe analyses. d) Framboids associated with carbonaceous material in LWC88 and maps of carbon (in red) and sulfur (in yellow). Scale bars are 10 µm. (For interpretation of the references to colour in this figure legend, the reader is referred to the web version of this article.)

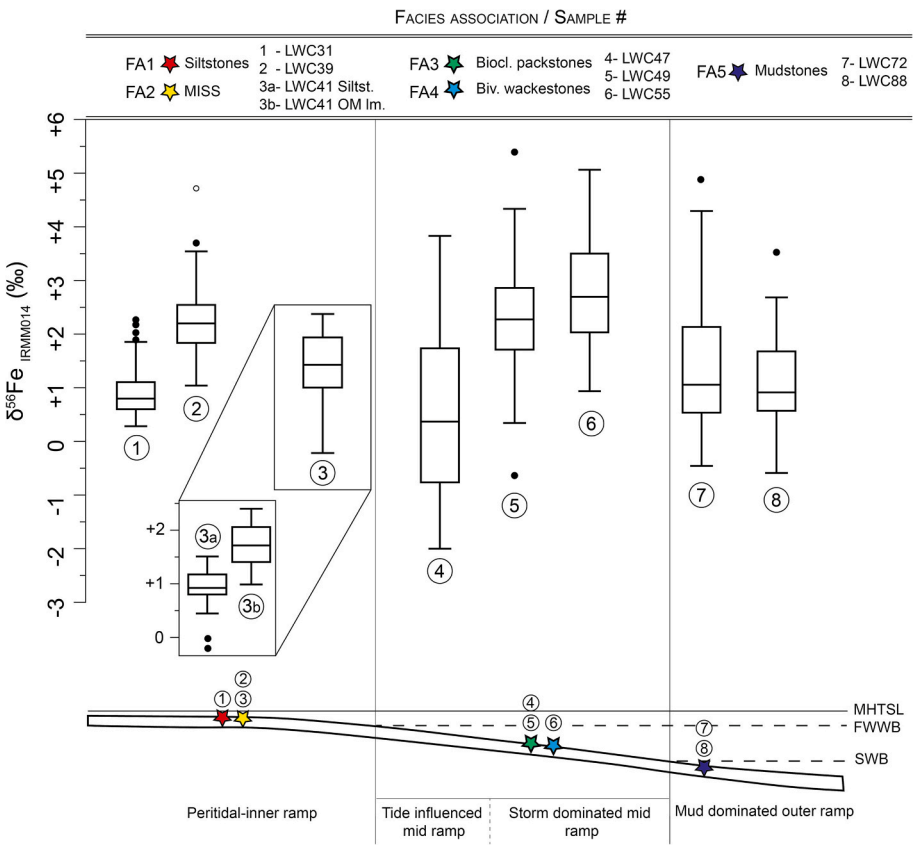

Fig. 6. Fe isotope compositions of pyrite from the Lower Weber Canyon section as a function of the depositional environment along a ramp system. The different star colors refer to the corresponding facies associations. Sample LWC31 is part of FA1 (red star). Samples LWC39 and LWC41 are MISS (FA2, yellow star). Please note that sample LWC41 encloses two facies in which pyrite is observed. The first is the silty part (reported as LWC41 Siltst.) and the second is the OM-rich laminae (noted LWC41 OM). F3 (green star) includes samples LWC47 and LWC49. Sample LWC55 is part of FA4 (blue star). Samples LWC72 and LWC88 are included in FA5 (purple star). Fe isotope compositions are reported using outlier box plot representation. Line through the box is the median and the edges of the box represent the quartiles (lower line is the 1st quartile Q1, i.e. the 25th percentile, and upper line is the 3rd quartile Q3, i.e. the 75th percentile). Lower and upper whiskers represent 1.5*IQR (interquartile range, i.e. the range between Q1 and Q3). The minimum and maximum are marked by small lines at the end of whiskers and represent respectively the lowest and highest values of the distribution, excluding outlier values of the dataset (filled and unfilled dots below and above whiskers). See Fig. 1 for abbreviations. (For interpretation of the references to colour in this figure legend, the reader is referred to the web version of this article.)

value of +1.32‰ (Fig. 6). In the mid ramp sediments (FA3 and FA4), the 125 $\delta^{56}Fe_{py}$ values display the largest range from −1.99 to +5.39‰, and an average $\delta^{56}Fe_{py}$ value of +2.10‰ (Fig. 6). Samples from inner and mid ramp systems display monomodal distributions (Fig. 7) for which median values are statistically different (Mann-Whitney p = 1.69E-10; Table S4). In the outer ramp deposits (FA5), $\delta^{56}Fe_{py}$ values (n = 82) range from −0.59 to +4.88‰, with an average $\delta^{56}Fe_{py}$ value of +1.28‰ (Fig. 6).

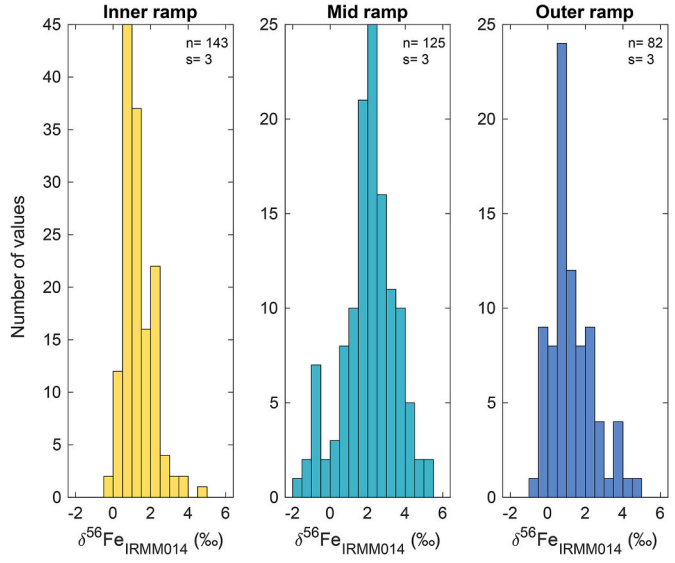

Fig. 7. Pyrite $\delta^{56}Fe$ distributions as a function of the domain of the ramp, i.e. the inner ramp, the mid ramp and the outer ramp system. The number of values (n), and the number of samples from which pyrite grains were measured (s) are indicated for each histogram.

In details, the inner ramp FA1 includes samples LWC31 (n = 77) and LWC41 Siltst. (n = 13). The Fe isotope compositions range from +0.28 to +2.27‰ in LWC31, and from −0.21 to +1.50‰, in LWC41 Siltst. (Fig. 6) and show similar distribution with the respective mean $\delta^{56}Fe_{py}$ values of +0.91‰ and + 0.84‰ (Mann-Whitney p = 0.662; Table S5). The inner ramp FA2 includes samples LWC39 (n = 30) and LWC41 OM (n = 23) with higher $\delta^{56}Fe$ values, varying respectively from +1.04 to +4.72‰ and from +0.98 to +2.39‰. These two samples display statistically different mean $\delta^{56}Fe$ values of +2.29‰ and + 1.71‰, respectively (t-test p = 2.7E-3; Table S5). Fe isotope compositions of mid ramp FA3, including samples LWC47 (n = 25) and LWC49 (n = 52), range from −1.99 to +3.83‰ and from −0.63 to +5.39‰. They display statistically different $\delta^{56}Fe_{mean}$ values of +0.46‰ and + 2.30‰, respectively (t-test p = 8.01E-9; Table S5). Mid ramp FA4 corresponds to sample LWC55 (n = 48), which shows $\delta^{56}Fe$ values ranging from +0.93 to +5.06‰, with the highest average $\delta^{56}Fe$ value of +2.73‰. Outer ramp FA5 is represented by samples LWC72 (n = 35) and LWC88 (n = 47). Pyrite grains in LWC72 have Fe isotope compositions ranging from −0.46 to +4.88‰. In LWC88, pyrite $\delta^{56}Fe$ values vary between −0.59 and + 3.52‰. These two samples show similar distribution with the respective mean $\delta^{56}Fe$ values of +1.55‰ and = +1.08‰ (Mann-Whitney p = 0.249; Table S5). No correlation between $\delta^{56}Fe$ values and S content or between $\delta^{56}Fe$ and $\delta^{34}S$ values has been observed (Fig. S5).

3.6. Iron isotope signatures, facies and pyrite morphologies

The Fe isotope variations can be represented as a function of the four pyrite morphologies (excepting the nodule from LWC31; Fig. 8). The $\delta^{56}Fe$ values of euhedral grains range between −1.14 to +5.06‰ (n = 131), with an average value of +1.66‰. Framboidal pyrite have a lower range of variations, with $\delta^{56}Fe$ values from −0.76 to +3.83‰ (n = 43) and a mean $\delta^{56}Fe$ value of +1.65‰. Aggregated pyrite grains show an Fe isotope range between −1.99 and + 5.39‰ (n = 103) and an average

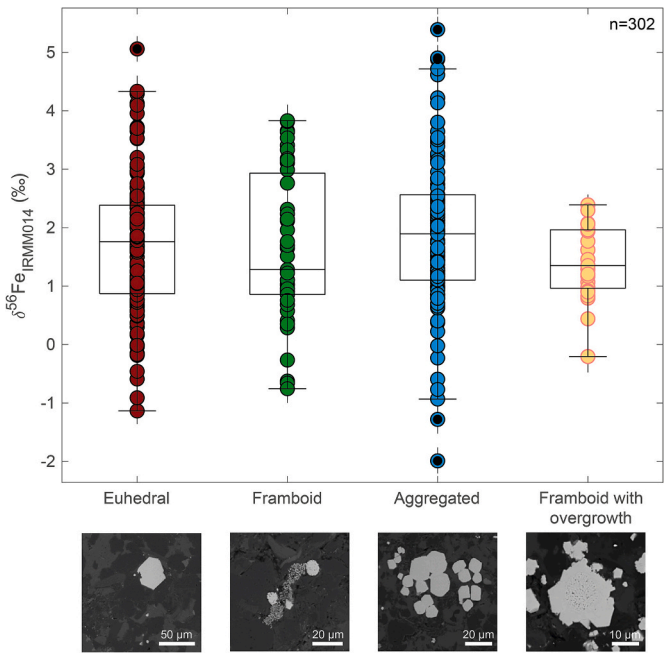

Fig. 8. $\delta^{56}Fe_{py}$ as a function of the morphology of pyrite grains. The different pyrite types are categorized as euhedral, framboids, aggregated and framboids with secondary overgrowth. No statistical differences are observed between each morphology.

δ^{56}Fe value of +1.89‰. The Fe isotope compositions of framboidal grains with secondary overgrowth range from −0.21 to +2.39‰ (n = 25). These grains display an average δ^{56}Fe value of +1.41‰. These four pyrite morphologies describe monomodal Gaussian-type distributions (Fig. S6) and the differences of mean δ^{56}Fe values are not statistically relevant (t-test p value = [0.082–0.929]; Table S6). Moreover, there is no significant differences in the mean δ^{56}Fe values between the core ($\delta^{56}Fe_{mean}$ = +1.38 ± 0.57‰) and the rim ($\delta^{56}Fe_{mean}$ = +1.48 ± 0.76‰) among the framboid with secondary overgrowth pyrite grains (Mann-Whitney p = 0.432). The observation of these 4 different pyrite types depends on the associated facies (Fig. 9):

- In FA1 (siltstones), pyrite grains are euhedral, aggregated, framboidal (with diagenetic overgrowth) or forming a nodule (Fig. 9). Euhedral pyrite grains have a mean δ^{56}Fe value of +1.20 ± 0.31‰ (n = 7). The aggregated grains display an average δ^{56}Fe value of +1.09 ± 0.44‰ (n = 28). The distributions observed for euhedral and aggregated pyrite in FA1 are monomodal and similar (Mann-Whitney p = 0.695; Table S7). Framboids with secondary overgrowth and the pyrite nodule show the respective mean δ^{56}Fe values of +0.69 ± 0.45‰ (n = 7) and + 0.77 ± 0.40‰ (n = 48). These two morphologies display monomodal and similar distributions (Mann-Whitney p = 0.640; Table S7). Moreover, the mean values observed in framboids with overgrowth and the nodule are lower than those observed in euhedral and aggregated grains. However, the difference in means between these two groups is covered by the uncertainties of the analyses (Fig. 9).
- Excluding the nodule, which has only been observed in FA1, the same pyrite morphologies are reported in FA2 (MISS; Fig. 9). Euhedral grains in FA2 show a monomodal distribution and a mean δ^{56}Fe value of +2.08 ± 0.59‰ (n = 24). In aggregated grains, the δ^{56}Fe values are distributed along a monomodal distribution on a larger range than euhedral grains. The average value is +2.50 ± 1.04‰ (n = 11). However, the difference between euhedral and aggregated grains is not statistically significative (t-test p = 0.137; Table S7). Framboidal pyrite with secondary overgrowth also displays a monomodal distribution, which is characterized by the lowest mean δ^{56}Fe value of +1.62 ± 0.54‰ (n = 26) among the other pyrite morphologies observed in FA2. However, once again the difference in means between the recrystallized framboids and the other pyrite types falls into the uncertainties of the analyses.
- The overgrowth affecting framboidal pyrite are no longer observed in FA3 (bioclastic packstones) and the other following facies (Fig. 9). Euhedral grains in FA3 have an average δ^{56}Fe value of +1.85 ± 1.30‰ (n = 22), which is similar to the Fe isotope signature of framboidal grains (+1.78 ± 1.42‰, n = 26). Aggregated grains have a slightly lower mean δ^{56}Fe value of +1.51 ± 1.59‰ (n = 29). The distributions of these 3 pyrite types spread over a larger range than those of FA1 and FA2 and are similar (Mann-Whitney p = [0.168–0.828]; Table S7).
- The three pyrite types described in FA3 are also observed in the following facies FA4 and FA5 (Fig. 9). Only one sample (LWC55) is part of FA4 (bivalve wackestones), in which pyrite grains record the highest Fe isotope compositions. Euhedral pyrite shows a sparse distribution with a mean δ^{56}Fe value of +2.92 ± 1.22‰ (n = 13). Five framboids were measured and display a mean δ^{56}Fe value of +2.47 ± 1.12‰. Aggregated grains show a monomodal distribution with an average Fe isotope composition of +2.70 ± 0.97‰ (n = 30). The isotopic differences between these three pyrite types are statistically insignificant (t-test p = [0.528–0.633]; Table S7).
- Samples from FA5 (mudstones) enclose euhedral pyrite grains, which describe an asymmetric distribution with a mean δ^{56}Fe value of +1.25 ± 1.08‰ (n = 65), framboids, characterized by a lower mean δ^{56}Fe value of +1.01 ± 0.80‰ (n = 12), and a few aggregated grains displaying a δ^{56}Fe value of +2.29 ± 2.09‰ (n = 5; Fig. 9). Yet, there is no significant difference between these distributions (Mann-Whitney p = [0.269–0.523]; Table S7).

Although some pyrite exhibits secondary features, i.e. recrystallization (Fig. 5a and b), their iron isotope compositions remain similar (Fig. 9). For example, there is no profile of variation of the δ^{56}Fe values in the framboidal pyrite with overgrowths. Overall, there is no clear difference of Fe isotope compositions between the pyrite types observed among each facies.

4. Discussion

4.1. Diagenetic and synsedimentary pyrite grains

Pyrite in three different facies (FA3, FA4, FA5) exhibits preserved primary morphological features such as framboids, characterized by an average size of 11 ± 5.0 µm (Fig. 4). The study of Rickard (2019), in line with the pioneer work of Wilkin and Barnes (1997), documented that diagenetic framboids yield a mean diameter of 6.7 µm, meaning that framboids from our samples most likely precipitated in the sediment porewaters. As framboids are closely associated with well-preserved carbonaceous materials, we suggest that the Fe isotope compositions of those grains are inherited from early diagenetic processes. The Fe isotope compositions (ranges and mean values) of these framboids is similar to the Fe isotope compositions of euhedral and aggregated grains within the same facies. Therefore, we can reasonably hypothesize that framboids, euhedral and aggregated pyrite formed in the sediments through the same precipitation event.

The presence of overgrowth around framboidal cores in FA1 and FA2 samples (LWC31, LWC39 and LWC41) marks a subsequent event of precipitation. Supposedly, pyrite resulting from secondary fluid circulation should display contrasting δ^{56}Fe values or different mineralogical features. However, the Fe isotope compositions of overgrowth are similar those of framboidal cores. Based on the fact that (1) there is also no significant isotopic difference between rimed framboidal pyrite and the other pyrite types (i.e. euhedral or aggregated pyrite) observed within the same facies (FA1 or FA2), and (2) in FA2 sample LWC41, an isotopic heterogeneity is preserved between pyrites from the silty

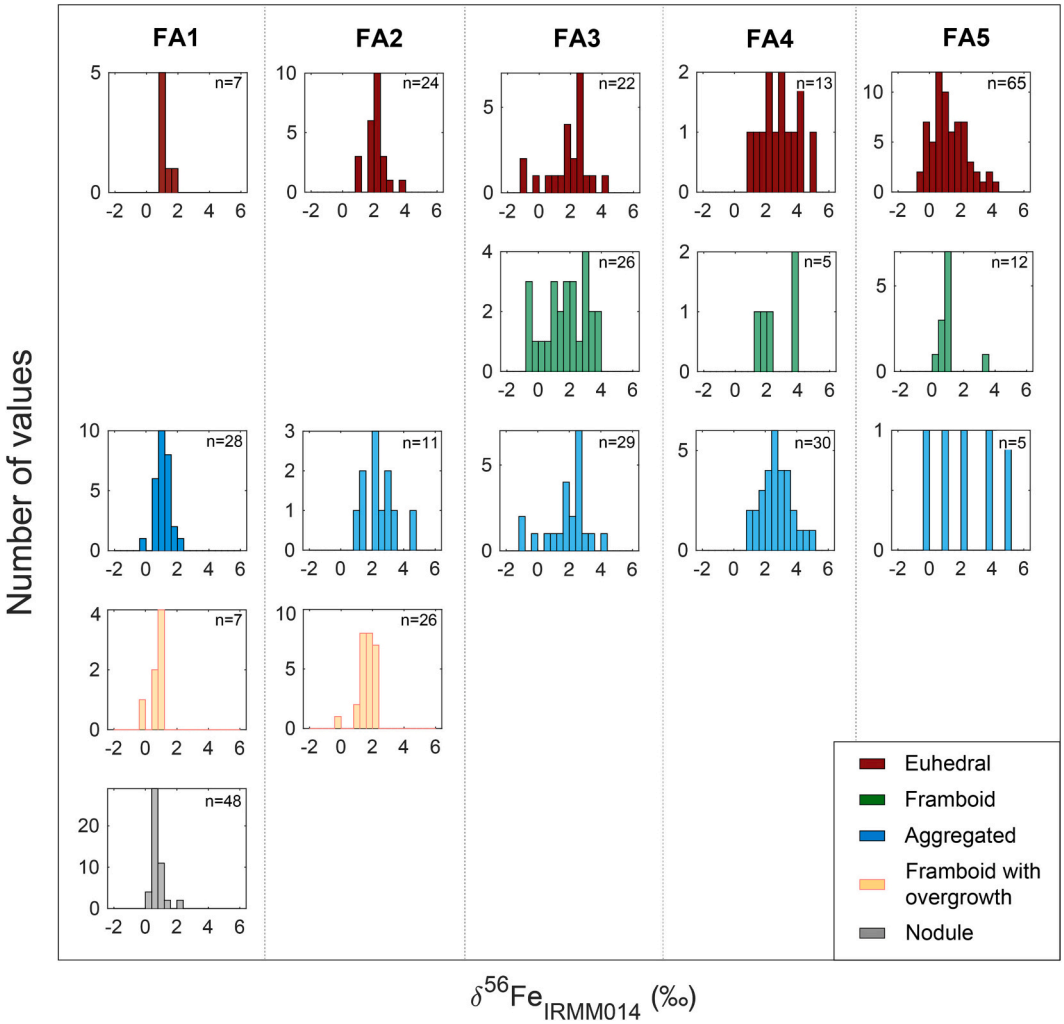

Fig. 9. Pyrite $\delta^{56}Fe$ distributions as a function of pyrite morphologies in each facies (FA1 to FA5). Data from euhedral pyrite are reported in red, from framboids in green, from aggregates in blue, from framboids with secondary rims in yellow and from the nodule in grey. The number of values (n) is indicated for each histogram. (For interpretation of the references to colour in this figure legend, the reader is referred to the web version of this article.)

sediments (LWC41 Siltst.) and pyrite from the organic laminae (LWC41 OM), we suggest that this secondary fluid circulation did not affect the Fe isotope compositions of the initial pyrite grains (framboid dissolution and recrystallization without additional Fe supply, i.e. low fluid/mineral ratio).

The influence of late diagenetic processes is illustrated by the isotope signatures of CAS. The comparison between the Fe and S isotope compositions of pyrite and the S isotope composition of CAS reveals that the variation of $\delta^{56}Fe$ and $\delta^{34}S_{py}$ values does not match with the S isotopic value of sulfate reservoir ($\delta^{34}S_{CAS}$; Fig. 3). The decoupling between pyrite and CAS means that the isotopic signatures of pyrite are not related to the evolution of the sulfate reservoir from which carbonate precipitate. This decoupling raises concerns about secondary overprint that could have affected CAS (Swart, 2015). In this study, $\delta^{34}S_{CAS}$ values were measured in samples characterized by Mn/Sr ratios between 11 and 40. Due to the decrease of Sr concentrations in carbonates during late/burial diagenetic processes, the Mn/Sr ratio is widely used to assess the degree of carbonate recrystallization. Consequently, samples showing high Mn/Sr ratio (> 2) reflect secondary alteration (Kaufman and Knoll, 1995; Derry, 2010). Here, the analyzed samples have minimum Mn/Sr ratio of 11 (Table S1), ratio showing an extensive carbonate recrystallization. Consequently, the $\delta^{34}S_{CAS}$ signal is likely inherited from late diagenetic processes.

Although late diagenetic processes occurred in the LWC samples, the association of pyrite with preserved organic materials and Fe isotope measurements indicate that most of the facies (FA1, FA3, FA4 and FA5) contain pyrite of early diagenetic origin. In FA2 (MISS), the presence of framboid remains within organic-rich laminae is suggestive of the formation of pyrite when biofilms were the site of metabolic activities, i.e. framboids of synsedimentary origin. Those pyrite grains have been partly recrystallized (i.e. overgrowth around framboids and euhedral grains) but still likely preserve their original Fe isotope compositions. Therefore, we propose that samples of the LWC section contain two generations of pyrite. The first generation represents synsedimentary pyrite associated with MISS (FA2), which formed during the activity of the biofilm close to the water column/sediment interface. The second generation is represented by early diagenetic pyrite (FA1, FA3, FA4 and FA5), whose formation is still controlled by a microbial activity spreading over the upper tens of centimeters of the sediments. Thus, synsedimentary to early diagenetic processes likely largely controlled Fe isotopic signatures of pyrites in the studied samples during the late Smithian and across the SSB.

4.2. Iron isotope kinetic and equilibrium isotope effects

Pyrite precipitation associated with various degrees of kinetic and equilibrium fractionation is a possible hypothesis to explain large Fe isotope range of isotopic composition (Mansor and Fantle, 2019). This

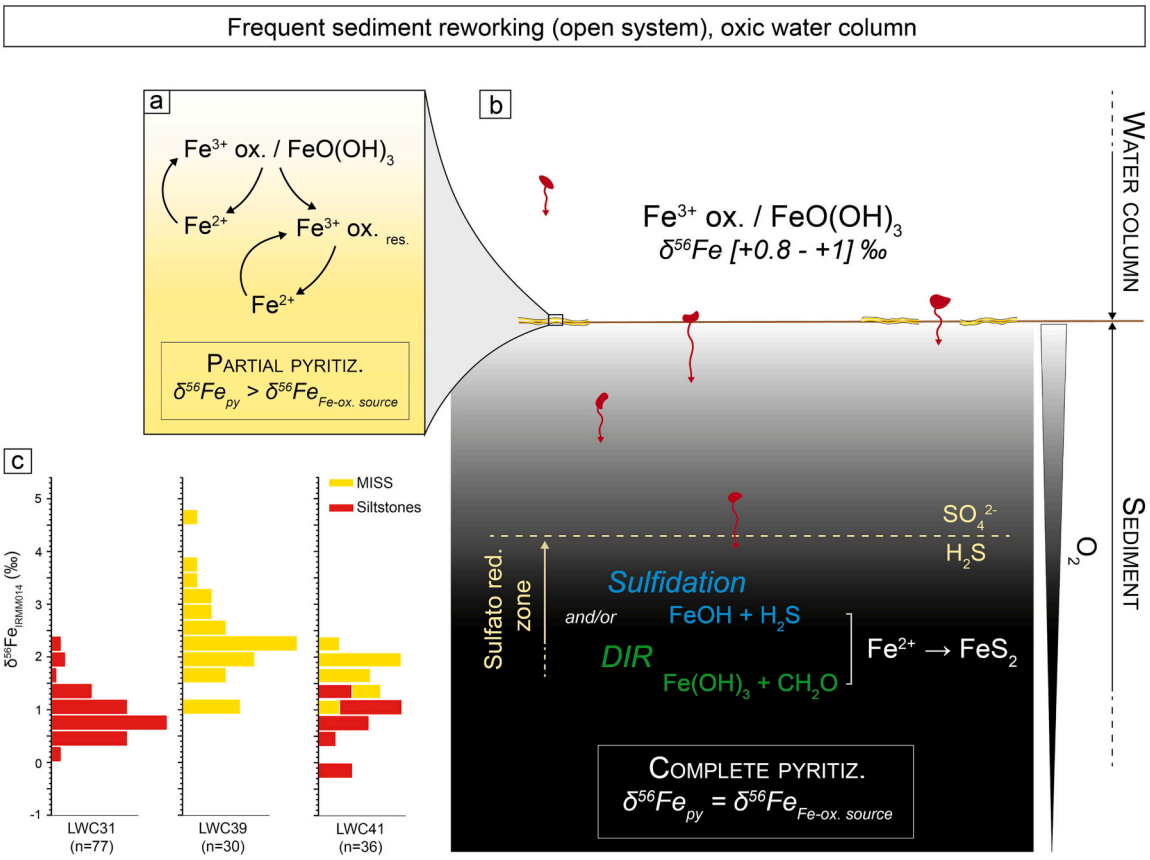

Fig. 10. Iron cycling model in the sediments from inner ramp samples. a) Model of Fe reduction for MISS samples (FA2), where a strong redox gradient occurs due to the variety of microbial metabolisms. In this case, Fe-oxides are partially reduced, and recycling can generate higher $\delta^{56}Fe$ values. b) Model of Fe reduction for siltstone samples (FA1). In this model, Fe-oxides are converted into Fe^{2+} or FeS and subsequently pyrite by reaction with H_2S. Sulfide is produced by microbial sulfate reduction (blue pathway: Sulfidation) combined with the possible effect of iron reducing bacteria (green pathway: Dissimilatory Iron Reduction). c) Pyrite $\delta^{56}Fe_{py}$ values distributions for the facies associations FA1 (siltstone) and FA2 (MISS). (For interpretation of the references to colour in this figure legend, the reader is referred to the web version of this article.)

hypothesis links Fe/S ratio changes with highly variable Fe pyrite isotope signatures. Indeed, an elevated Fe/S ratio enhances the expression of kinetic fractionation, i.e. formation of pyrite with negative $\delta^{56}Fe$ values, in a sulfate (and thus sulfide) poor environment. In contrast, pyrite expressing the equilibrium isotope fractionation, i.e. positive $\delta^{56}Fe$ values, reflects low Fe/S ratio and thus an environment with higher sulfate concentrations. Therefore, the increase of $\delta^{56}Fe$ values through the SSB can reflect variations in the supply of sulfate to the ocean, for example by volcanic degassing as already suggested during the SSB interval (Bond and Grasby, 2017). In this latter case, the absence of high Hg concentrations through the SSB does not support sulfate concentration variations driven by volcanism. Finally, although not entirely excluded, the absence of covariation between the sulfur content and pyrite $\delta^{56}Fe$ values or between pyrite $\delta^{56}Fe$ and $\delta^{34}S$ values rather suggests that sulfur availability during pyritization did not primarily control the $\delta^{56}Fe$ signal observed in the studied samples through the SSB.

4.3. Pyrite $\delta^{56}Fe$ values controlled by sedimentary depositional settings and microbial communities

We suggest that $\delta^{56}Fe$ variability is driven by redox cycling proceeding within the sediment, including biotic Fe-oxide reduction by microorganisms, a process named dissimilatory iron reduction (DIR), and reductive dissolution of Fe-oxides by sulfides. Pyrite Fe isotope signatures may also partly reflect kinetic and equilibrium isotope effect as the reductive dissolution of Fe-oxides likely change, at a local scale, the Fe/S ratio. The petrographic observations (Fig. 1), $\delta^{34}S_{py}$ values (Fig. 3) and $\delta^{56}Fe$ values (Fig. 7) allow to identify two endmembers. Both endmembers are largely dependent of the degree of connectivity of the sediment porewaters with the overlying water column, this latter likely being fully oxygenated as suggested by the relatively low S content (mean S content = 2585 ppm) and a low TOC content (mean TOC = 1477 ppm), which are not expected under euxinic or anoxic conditions (Lyons et al., 2009 for a review). Endmember 1 is depicted in samples from the inner ramp system. In these samples, the negative $\delta^{34}S_{py}$ (Fig. 3) and the disturbed OM-rich laminae (Fig. S7) suggest a good ventilation of the sediments, leading to a constant replenishment of the S and Fe reservoirs. However, this parameter alone does not explain the variability of $\delta^{56}Fe$ values. Because samples enclosing MISS have mean $\delta^{56}Fe$ values significatively different from siltstones, we suggest that the activity of microorganisms concentrated in MISS (only) influence the Fe isotope signatures of pyrite through the re-cycling of Fe species. Endmember 2 is illustrated by samples from the mid and outer ramp system. In these samples, $\delta^{34}S_{py}$ are positive (Fig. 3) and the position along the ramp suggests that the sediments are dominated by a relatively low energy regime. The increasing trend described by both $\delta^{34}S_{py}$ and $\delta^{56}Fe$ suggest that pyrite record diagenetic processes occurring under closed system in the sediment porewaters.

Therefore, two models are proposed below to account for the $\delta^{56}Fe$ variations observed within the LWC ramp system deposits: (1) an "inner ramp" model, functioning in an open system (i.e. frequent sediment reworking leading to a good connection between the sediment porewaters and the overlying water column) and (2) a "mid and outer ramp"

model, operating in a closed system (i.e. rare sediment reworking leading to a disconnection between the sediment porewaters and the overlying water column) and allowing the buildup of Fe-oxide pools within the sediments.

4.3.1. Inner ramp model: δ^{56}Fe values controlled by the nature of deposit

The LWC inner ramp is characterized by frequent remobilization of sediments by tidal currents or waves and bioturbation that facilitated the connection between sediment porewaters and the overlying water column. Therefore, sulfate, Fe-oxides and organic matter that fuel metabolic reactions related to sedimentary sulfides precipitation are assumed to be non-limiting. An open system is consistent with obtained negative δ^{34}S values in average ($\delta^{34}S = -11.4 \pm 9.3‰$, 1SD) and specifically in samples LWC31, LWC39 and LWC41 (average δ^{34}S value $= -18.4 \pm 1.6‰$, 1SD), which were also measured for their Fe isotope compositions. Consequently, δ^{56}Fe values of $+2.04 \pm 0.72‰$ (1SD) associated with MISS samples (FA2; LWC39 and LWC41 OM; Fig. 10a and c) suggest that a strong redox gradient developed in these microbial mats where iron reduction and oxidation can occur cyclically or even simultaneously (Byrne et al., 2015; Berg et al., 2016) due to the co-localized presence of aerobic and anaerobic metabolisms (e.g. O_2 respiration, H_2S oxidizers and sulfate reducers; Kühl and Jørgensen, 1992), fostered by bioturbation (Fig. S7). In the case of well-ventilated sediments, a partial reduction of the Fe-oxide reservoir is suggested (Fig. 10a), owing strong redox fluctuations within a biofilm that can occur rapidly within restricted areas (Fike et al., 2008; Dupraz et al., 2009). This process should produce (1) a ^{56}Fe-depleted Fe(II) pool available for pyrite precipitation, and (2) a ^{56}Fe-enriched residual Fe-oxide pool. Depending on the redox gradient, the reduction of the residual heavy Fe-oxide reservoir can also occur, as well as a complete or partial re-oxidation of the newly formed pyrite. This cryptic Fe cycle can produce heavy pyrite δ^{56}Fe values associated with a large isotopic range, comparable to those observed in FA2.

On the other side, pyrites from inner ramp siltstones (FA1; LWC31 and LWC41 Siltst.) display an average pyrite δ^{56}Fe value of $+0.90‰$, which matches with the canonical Fe isotope compositions known for Fe-oxides through Earth history (Rouxel et al., 2005; Wu et al., 2011; Fig. 10b and c). Therefore, we hypothesize that these pyrite grains record the isotope composition of the initial Fe-oxide source. In well-ventilated sediments devoid of biofilms, microbial sulfate reduction (MSR) occurs deeper in the sediments where the quantity and reactivity of organic matter decrease as a function of the sediment depth and redox potential (Middelburg, 1989; Dauwe et al., 1999; Meister et al., 2013). Moreover, due to its low mobility, Fe-oxide quantity decreases as a function of the sediment depth. In this case, even limited by the low reactivity of organic matter (i.e. at a lower rate of sulfate reduction), the

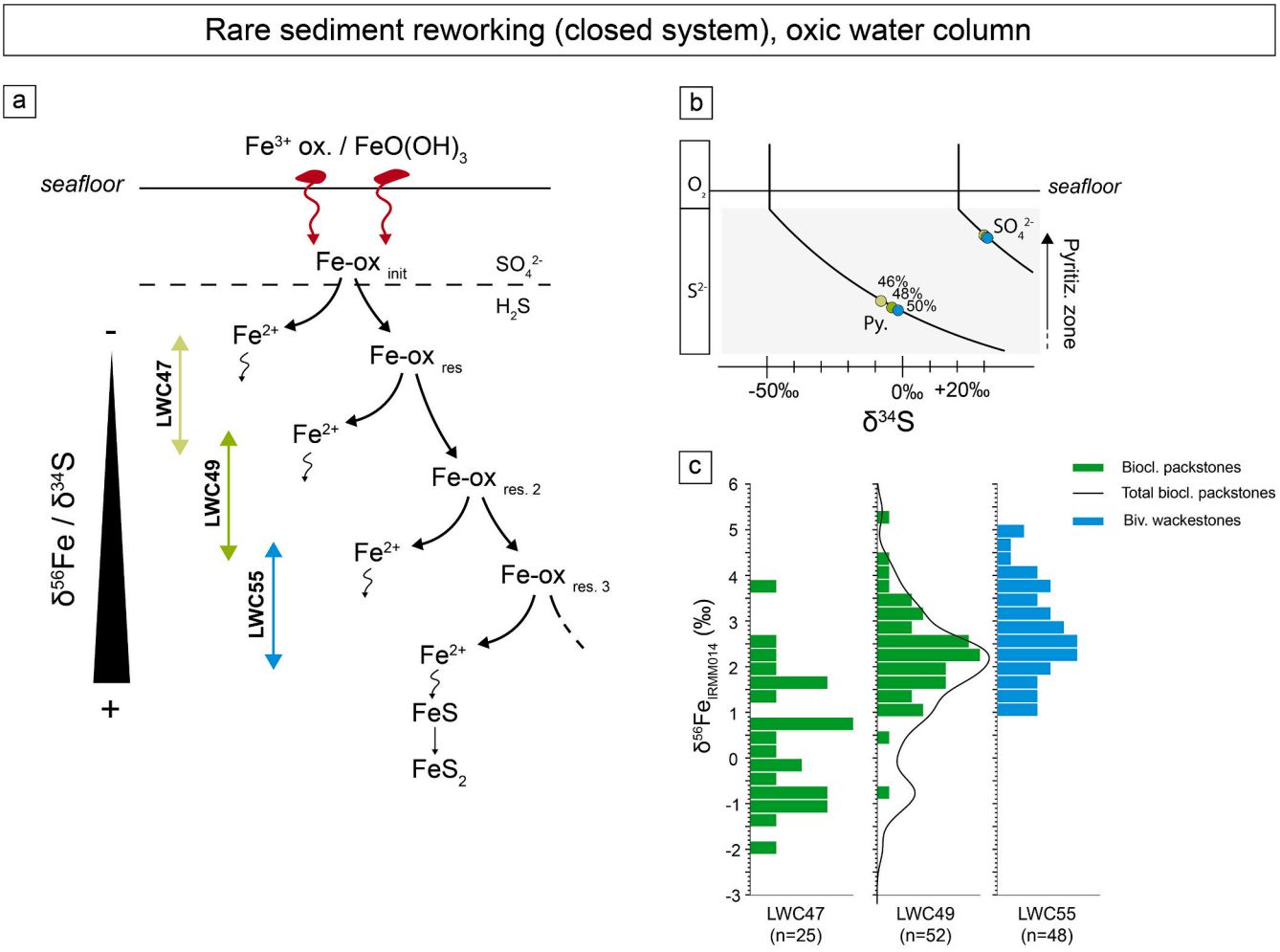

Fig. 11. Iron cycling model in the sediments from mid and outer ramp samples. a) Model for Fe-oxide reduction in closed-system, where Fe-oxides are partially reduced by reaction with limiting H_2S (as sulfate reservoir also evolves in a closed-system), leading to the buildup of different residual Fe-oxide pools. b) Evolution of newly formed pyrite and sulfate in a closed sediment. Percentage of newly formed pyrite during the Rayleigh process is reported for LWC 47 (light green), LWC49 (green) and LWC55 (blue). c) Pyrite δ^{56}Fe distributions for samples from FA3 and F4. Green and blue colors correspond to facies associations FA3 (bioclastic packstones) and FA4 (bivalve wackestones) respectively. Black line represents probability density for both LWC47 and LWC49. (For interpretation of the references to colour in this figure legend, the reader is referred to the web version of this article.)

production of H_2S through MSR balances or exceeds the rate of Fe-oxide consumption. Therefore, a total reduction of Fe-oxide is expected to account for the observed iron isotopic signatures. Dissimilatory iron reduction (DIR) is however not suggested here because $\delta^{56}Fe_{py}$ values are not negative enough to support this process (Crosby et al., 2005; Fig. 10b).

4.3.2. Mid and outer ramp model: $\delta^{56}Fe_{py}$ controlled by H_2S production in a closed-system

Samples from the mid ramp system record a progressive increase in $\delta^{56}Fe$ values, from +0.46 to +2.73‰, that is also recorded in S isotope compositions with an increase from −8.2 to −2.8‰ (Fig. 3). A concurrent increase of $\delta^{56}Fe$ and $\delta^{34}S$ values for mid ramp samples can reflect a consumption of the Fe-oxide and sulfate reservoirs within the sediments under closed system conditions relative to the overlying water column (Fig. 11). Samples LWC47 and LWC49 show disarticulated bioclasts of bivalves and ammonoids, reflecting rare storm events and limited transport (Seilacher et al., 1985; Kidwell et al., 1986; Grosjean et al., 2018). LWC55 also shows fragmented bivalves and thin layers of silty beds (Fig. 1), but the higher proportion of micritic matrix compared to LWC47 and LWC49 suggests a slightly deeper depositional environment (Fig. 1). In such environments, episodic storms resulted in rapid sediment accumulations that promoted disconnections between porewaters and the water column. In this environmental context replenishment of solute oxidized species is restricted (Fig. 11a). Consequently, a closed system sulfate reduction developed and may have driven the partial reduction of Fe-oxides, leading to the buildup of a residual Fe-oxide pools in the sediments that are progressively ^{56}Fe-enriched (Fig. 11a and b). The large range and non-Rayleigh-type distribution of $\delta^{56}Fe$ values in LWC47 (Fig. 11c) support that (1) pyrite recorded multiple steps of partial reduction of a residual Fe-oxide pool, and (2) a possible recycling (reoxidation-reduction) of the produced Fe^{2+}.

The average $\delta^{56}Fe$ value of outer ramp samples LWC72 and LWC88 is of +1.28‰, i.e. ~1‰ lower than that of the mid ramp samples (mean $\delta^{56}Fe_{Mid} = +2.10$‰). The large variability of ±1.14‰ observed in these outer ramp samples is not distributed along a Rayleigh-type process. In contrast, S isotope signal increases, from −4.0‰ in the mid ramp to +6.4‰ in the outer ramp setting. LWC72 and LWC88 pertained to FA5 (Fig. 6), which is dominated by sediment decantation and very low hydrodynamic regime. Deposition of FA5 occurred in a more distal position along the ramp where sediment reworking is very rare, meaning that the sediments likely evolved under closed system conditions. In such setting, sulfides generated in sediments by sulfate reduction may promote the partial reduction of reactive Fe-oxides (Fig. 11) in outer ramp sediments. This partial reduction produces Fe^{2+} that can be then converted into pyrite. Due to the activity of sulfate reducing metabolisms and the progressive buildup of residual Fe-oxide pools from an initial reservoir, reactive Fe-oxides tend to be rare. Therefore, sulfides produced deeper in the sediments are not consumed in situ by reaction with Fe^{2+} and accumulate, leading to a diffusion upward its zone of production (Riedinger et al., 2017; Liu et al., 2020). Hypothetically, this diffusing sulfide flux may be generated at the sulfate-methane transition zone (SMTZ), as recent studies documented the precipitation of ^{34}S-enriched pyrite in this deeper area in sediments (Liu et al., 2020; Pasquier et al., 2021). However, the data presented here are not conclusive evidence for the existence of a paleo-SMTZ in this ramp system. This diffusion process results in the successive sulfidation of the (more) reactive residual and initial Fe-oxides pools (Fig. 11), converting them to pyrite characterized by ^{34}S-enriched S isotope signatures, a large $\delta^{56}Fe$ range of values and an average $\delta^{56}Fe$ signal close to the signatures of the Fe-oxide source.

4.3.3. Pyrite formation during an interval of biotic diversity loss: A depositional environment control rather than deleterious anoxic conditions

The oceanic redox conditions through the SSB were often documented by studying pyrite. Indeed, many studies focused on the occurrence and size distribution of pyrite framboids, Fe speciation and multiple sulfur isotope signals to assess euxinia, anoxia or ferruginous conditions of the water column (e.g. Shen et al., 2011; Sun et al., 2015; Clarkson et al., 2016; Song et al., 2019; Dai et al., 2021). However, there have been no studies using iron isotopes to document this biotic crisis, although iron is also a redox-sensitive element. Here we evidence that these depositional environments and more specifically the degree of sediment connection with the water column, which is modulated by sediment accumulation and reworking, controlled the S and Fe isotopic compositions through variations of Fe-oxide and sulfate supply in the sediment microbial active zones. When sediments are well-connected to the water column, pyrite displays negative $\delta^{34}S$ values and Fe isotope compositions reflect the complete reduction of Fe-oxides. On the other hand, the disconnection between the water column and the sediments leads to the isotopic consumption of sulfate and Fe-oxide reservoirs.

The control of the sediment-seawater connectivity between each depositional environment is well evidenced by the S isotope signatures, while Fe isotopes show the additional influence of the nature of deposit (presence of MISS) in the inner ramp system and the reactivity of Fe-oxides with H_2S fluxes in the outer ramp system. This suggests that both Fe and S isotopic variations through the SSB at LWC are driven by local processes within the sediments rather than the water column redox structure. In this study, no direct causality can be established between Fe isotopic signal and interval of biotic crisis, as already shown through the SSB using multiple sulfur isotope signals (Thomazo et al., 2019). Finally, the combination of Fe isotope compositions along with S isotopes and petrographic observations is consistent with local microbial and sedimentological processes as primary drivers of sedimentary geochemical signals within the studied biotic diversity loss interval.

5. Conclusions

Pyrite Fe isotope compositions obtained from LWC through the Smithian-Spathian transition indicate a sedimentary depositional system control, locally coupled with an influence of the nature of deposits (i.e. the presence or absence of MISS) on pyrite formation. LWC sediments deposited along a tide and wave influenced ramp system, ranging from shallow inner ramp to deeper outer ramp settings, was overlaid by an oxygenated water column. In these environments, the intensity of biological and physical induced sediment reworking produces two regimes of water column-sediment exchanges, an open-system characterized by well-ventilated sediments and a closed-system govern by diffusion within the porewater sediment. We propose two iron cycling models both influenced by the position along the ramp and nature of the deposits. The first model is relevant to reworked sediments from inner ramp settings, where lighter $\delta^{56}Fe_{py}$ ($\delta^{56}Fe_{mean} \sim +1$‰) reflect the complete reduction of Fe-oxides and higher $\delta^{56}Fe_{py}$ values ($\delta^{56}Fe_{mean} \sim +2$‰) in MISS are attributed to a complex microbial oxidation-reduction cycling. The second model is relevant for sediments deposited in the mid and outer ramp zones that were rarely affected by reworking. The concurrent increase of Fe and S isotope compositions suggests that the disconnection between the sediment porewaters and water column drives the consumption of the Fe-oxide and sulfate sedimentary reservoirs.

This study highlights the importance of using different isotope systematics the sedimentary depositional/nature of sediments to unravel local versus global control on geochemical signatures and call for caution in the "redox" interpretation of Fe and S isotopic signals, especially digging into geological intervals associated with extensive oceanic anoxia.

Declaration of Competing Interest

The authors declare the following financial interests/personal relationships which may be considered as potential competing interests:

Johanna Marin-Carbonne reports financial support was provided by

Horizon 2020 European Innovation Council Fast Track to Innovation.

Data availability

Data will be made available on request.

Acknowledgements

K.G. Bylund, J.F. Jenks, D.A. Stephen, E. Fara, G. Escarguel, E. Vennin, G. Caravaca and A.S. Grosjean are thanked for their work in the field, and notably for their participation to the sample collection. We gratefully thank V. Pasquier for fruitful discussions, J. Alleon for his assistance during Raman analyses and M. Robyr for his help during EPMA analyses. We thank private landowners (Scott Rees – south side of Weber River and Mrs. Monte Brough – north side of Weber River) for allowing access to their lands. We thank Prof. T. Algeo and an anonymous reviewer for their helpful and constructive reviews of this paper. This research was supported by the European Union's Horizon H2020 research and innovation program ERC (STROMATA, grant agreement 759289). This work is also a contribution to the ANR project AFTER (ANR-13-JS06-0001-01) and was also supported by the French "Investissements d'Avenir" program, project ISITE-BFC (ANR-15-IDEX-03) and received funding from the programme TelluS of the Institut National des Sciences de l'Univers, CNRS.

Appendix A. Supplementary data

Supplementary data to this article can be found online at https://doi.org/10.1016/j.palaeo.2023.111507.

References

Adatte, T., Stinnesbeck, W., Keller, G., 1996. Lithostratigraphic and mineralogic correlations of near K/T boundary clastic sediments in northeastern Mexico: Implications for origin and nature of deposition. In: The Cretaceous-Tertiary Event and Other Catastrophes in Earth History. Geological Society of America. https://doi.org/10.1130/0-8137-2307-8.211.

Algeo, T.J., Kuwahara, K., Sano, H., Bates, S., Lyons, T., Elswick, E., Hinnov, L., Ellwood, B., Moser, J., Maynard, J.B., 2011. Spatial variation in sediment fluxes, redox conditions, and productivity in the Permian-Triassic Panthalassic Ocean. Palaeogeogr. Palaeoclimatol. Palaeoecol. 308, 65–83. https://doi.org/10.1016/j.palaeo.2010.07.007.

Archer, C., Vance, D., 2006. Coupled Fe and S isotope evidence for Archean microbial Fe (III) and sulfate reduction. Geology 34, 153. https://doi.org/10.1130/G22067.1.

Beatty, T.W., Zonneveld, J.P., Henderson, C.M., 2008. Anomalously diverse Early Triassic ichnofossil assemblages in northwest Pangea: a case for a shallow-marine habitable zone. Geology 36, 771–774. https://doi.org/10.1130/G24952A.1.

Behar, F., Beaumont, V., Penteado, H.L., 2001. Rock-Eval 6 Technology: Performances and Developments. Oil Gas Sci. Technol. 56, 111–134. https://doi.org/10.2516/ogst:2001013.

Berg, J.S., Michellod, D., Pjevac, P., Martinez-Perez, C., Buckner, C.R.T., Hach, P.F., Schubert, C.J., Milucka, J., Kuypers, M.M.M., 2016. Intensive cryptic microbial iron cycling in the low iron water column of the meromictic Lake Cadagno. Environ. Microbiol. 18, 5288–5302. https://doi.org/10.1111/1462-2920.13587.

Beyssac, O., Goffé, B., Chopin, C., Rouzaud, J.N., 2002. Raman spectra of carbonaceous material in metasediments: a new geothermometer. J. Metamorph. Geol. 20, 859–871. https://doi.org/10.1046/j.1525-1314.2002.00408.x.

Bond, D.P.G., Grasby, S.E., 2017. On the causes of mass extinctions. Palaeogeogr. Palaeoclimatol. Palaeoecol. 478, 3–29. https://doi.org/10.1016/j.palaeo.2016.11.005.

Bond, D.P.G., Wignall, P.B., 2010. Pyrite framboid study of marine Permian-Triassic boundary sections: a complex anoxic event and its relationship to contemporaneous mass extinction. Bull. Geol. Soc. Am. 122, 1265–1279. https://doi.org/10.1130/B30042.1.

Brayard, A., Bucher, H., Escarguel, G., Fluteau, F., Bourquin, S., Galfetti, T., 2006. The Early Triassic ammonoid recovery: Paleoclimatic significance of diversity gradients. Palaeogeogr. Palaeoclimatol. Palaeoecol. 239, 374–395. https://doi.org/10.1016/j.palaeo.2006.02.003.

Brayard, A., Vennin, E., Olivier, N., Bylund, K.G., Jenks, J., Stephen, D.A., Bucher, H., Hofmann, R., Goudemand, N., Escarguel, G., 2011. Transient metazoan reefs in the aftermath of the end-Permian mass extinction. Nat. Geosci. 4, 693–697. https://doi.org/10.1038/ngeo1264.

Brayard, A., Bylund, K.G., Jenks, J.F., Stephen, D.A., Olivier, N., Escarguel, G., Fara, E., Vennin, E., 2013. Smithian ammonoid faunas from Utah: implications for Early Triassic biostratigraphy, correlation and basinal paleogeography. Swiss J. Palaeontol. 132, 141–219. https://doi.org/10.1007/s13358-013-0058-y.

Brayard, A., Krumenacker, L.J., Botting, J.P., Jenks, J.F., Bylund, K.G., Fara, E., Vennin, E., Olivier, N., Goudemand, N., Saucède, T., Charbonnier, S., Romano, C., Doguzhaeva, L., Thuy, B., Hautmann, M., Stephen, D.A., Thomazo, C., Escarguel, G., 2017. Unexpected Early Triassic marine ecosystem and the rise of the Modern evolutionary fauna. Sci. Adv. 3 https://doi.org/10.1126/sciadv.1602159.

Brayard, A., Olivier, N., Vennin, E., Jenks, J.F., Bylund, K.G., Stephen, D.A., McShinsky, D., Goudemand, N., Fara, E., Escarguel, G., 2020. New middle and late Smithian ammonoid faunas from the Utah/Arizona border: New evidence for calibrating Early Triassic transgressive-regressive trends and paleobiogeographical signals in the western USA basin. Glob. Planet. Chang. 192, 103251 https://doi.org/10.1016/j.gloplacha.2020.103251.

Brayard, A., Jenks, J.F., Bylund, K.G., Olivier, N., Vennin, E., Stephen, D.A., Escarguel, G., Fara, E., 2021. Latest Smithian (Early Triassic) ammonoid assemblages in Utah (western USA basin) and their implications for regional biostratigraphy, biogeography and placement of the Smithian/Spathian boundary. Geobios 69, 1–23. https://doi.org/10.1016/j.geobios.2021.05.003.

Burchfiel, B., Davis, G.A., 1975. Nature and controls of Cordilleran orogenesis, Western United States: extensions of an earlier synthesis. Am. J. Sci. 275, 363–396.

Busigny, V., Planavsky, N.J., Jézéquel, D., Crowe, S., Louvat, P., Moureau, J., Viollier, E., Lyons, T.W., 2014. Iron isotopes in an Archean ocean analogue. Geochim. Cosmochim. Acta 133, 443–462. https://doi.org/10.1016/j.gca.2014.03.004.

Byrne, J.M., Klueglein, N., Pearce, C., Rosso, K.M., Appel, E., Kappler, A., 2015. Redox cycling of Fe(II) and Fe(III) in magnetite by Fe-metabolizing bacteria. Science 1979 (347), 1473–1476. https://doi.org/10.1126/science.aaa4834.

Caravaca, G., Brayard, A., Vennin, E., Guiraud, M., le Pourhiet, L., Grojean, A.-S., Thomazo, C., Olivier, N., Fara, E., Escarguel, G., Bylund, K.G., Jenks, J.F., Stephen, D.A., 2018. Controlling factors for differential subsidence in the Sonoma Foreland Basin (Early Triassic, western USA). Geol. Mag. 155, 1305–1329. https://doi.org/10.1017/S0016756817000164.

Clarkson, M.O., Wood, R.A., Poulton, S.W., Richoz, S., Newton, R.J., Kasemann, S.A., Bowyer, F., Krystyn, L., 2016. Dynamic anoxic ferruginous conditions during the end-Permian mass extinction and recovery. Nat. Commun. 7, 12236. https://doi.org/10.1038/ncomms12236.

Collin, P.Y., Kershaw, S., Tribovillard, N., Forel, M.B., Crasquin, S., 2015. Geochemistry of post-extinction microbialites as a powerful tool to assess the oxygenation of shallow marine water in the immediate aftermath of the end-Permian mass extinction. Int. J. Earth Sci. 104, 1025–1037. https://doi.org/10.1007/s00531-014-1125-3.

Crosby, H.A., Johnson, C.M., Roden, E.E., Beard, B.L., 2005. Coupled Fe(II)−Fe(III) Electron and Atom Exchange as a Mechanism for Fe Isotope Fractionation during Dissimilatory Iron Oxide Reduction. Environ. Sci. Technol. 39, 6698–6704. https://doi.org/10.1021/es0505346.

Dai, X., Yuan, Z., Brayard, A., Li, M., Liu, X., Jia, E., Du, Y., Song, H., Song, H., 2021. Calibrating the late Smithian (Early Triassic) crisis: New insights from the Nanpanjiang Basin, South China. Glob. Planet. Chang. 201, 103492 https://doi.org/10.1016/j.gloplacha.2021.103492.

Dai, X., Davies, J.H., Yuan, Z., Brayard, A., Ovtcharova, M., Xu, G., Liu, X., Smith, C.P.A., Schweitzer, C.E., Li, L., Perrot, M.G., Jiang, S., Miao, L., Coa, Y., Bai, R., Wang, F., Guo, W., Song, H., Tian, L., Dal Corso, J., Liu, Y., Chu, D., Song, H., 2023. A Mesozoic fossil lagerstätte from 250.8 million years ago shows a modern-type marine ecosystem. Science 379, 567–572. https://doi.org/10.1126/science.adf1622.

Dauwe, B., Middelburg, J.J., Herman, P.M., Heip, C.H., 1999. Linking diagenetic alteration of amino acids and bulk organic matter reactivity. Limnol 44, 1809–1814.

Decraene, M.N., Marin-Carbonne, J., Bouvier, A.S., Villeneuve, J., Bouden, N., Luais, B., Deloule, E., 2021. High-spatial-resolution measurements of iron isotopes in pyrites by secondary ion mass spectrometry using the new Hyperion-II radio-frequency plasma source. Rapid Commun. Mass Spectrom. 35 https://doi.org/10.1002/rcm.8986.

Derry, L.A., 2010. A burial diagenesis origin for the Ediacaran Shuram–Wonoka carbon isotope anomaly. Earth Planet. Sci. Lett. 294, 152–162. https://doi.org/10.1016/j.epsl.2010.03.022.

Dickinson, W.R., 2013. Phanerozoic palinspastic reconstructions of Great Basin geotectonics (Nevada-Utah, USA). Geosphere 9, 1384–1396. https://doi.org/10.1130/GES00888.1.

Dupraz, C., Reid, R.P., Braissant, O., Decho, A.W., Norman, R.S., Visscher, P.T., 2009. Processes of carbonate precipitation in modern microbial mats. Earth Sci. Rev. https://doi.org/10.1016/j.earscirev.2008.10.005.

Elrick, M., Polyak, V., Algeo, T.J., Romaniello, S., Asmerom, Y., Herrmann, A.D., Anbar, A.D., Zhao, L., Chen, Z.Q., 2017. Global-ocean redox variation during the middle-late Permian through Early Triassic based on uranium isotope and Th/U trends of marine carbonates. Geology 45, 163–166. https://doi.org/10.1130/G38585.1.

Embry, A.F., 1997. Global sequence boundaries of the Triassic and their identification in the Western Canada Sedimentary Basin 1. Bull. Can. Petrol. Geol. 45, 415–433.

Espitalié, J., Deroo, G., Marquis, F., 1985. La pyrolyse Rock-Eval et ses applications. Deuxième partie. Rev. l'Inst. Franç. Pétrol. 40, 755–784. https://doi.org/10.2516/ogst:1985045.

Fike, D.A., Gammon, C.L., Ziebis, W., Orphan, V.J., 2008. Micron-scale mapping of sulfur cycling across the oxycline of a cyanobacterial mat: a paired nanoSIMS and CARD-FISH approach. ISME J. 2, 749–759. https://doi.org/10.1038/ismej.2008.39.

Galfetti, T., Bucher, H., Ovtcharova, M., Schaltegger, U., Brayard, A., Brühwiler, T., Goudemand, N., Weissert, H., Hochuli, P.A., Cordey, F., Guodun, K., 2007. Timing of the Early Triassic carbon cycle perturbations inferred from new U–Pb ages and ammonoid biochronozones. Earth Planet. Sci. Lett. 258, 593–604. https://doi.org/10.1016/j.epsl.2007.04.023.

Goudemand, N., Romano, C., Leu, M., Bucher, H., Trotter, J.A., Williams, I.S., 2019. Dynamic interplay between climate and marine biodiversity upheavals during the early Triassic Smithian -Spathian biotic crisis. Earth Sci. Rev. https://doi.org/10.1016/j.earscirev.2019.01.013.

Grasby, S.E., Beauchamp, B., Embry, A., Sanei, H., 2013. Recurrent Early Triassic Ocean anoxia. Geology 41, 175–178. https://doi.org/10.1130/G33599.1.

Gregory, D.D., Large, R.R., Halpin, J.A., Baturina, E.L., Lyons, T.W., Wu, S., Danyushevsky, L., Sack, P.J., Chappaz, A., Maslennikov, V., Bull, S.W., 2015. Trace element content of sedimentary Pyrite in Black Shales. Econ. Geol. 110, 1389–1410. https://doi.org/10.2113/econgeo.110.6.1389.

Gröger, J., Franke, J., Hamer, K., Schulz, H.D., 2009. Quantitative recovery of elemental sulfur and improved selectivity in a Chromium-Reducible sulfur distillation. Geostand. Geoanal. Res. 33, 17–27. https://doi.org/10.1111/j.1751-908X.2009.00922.x.

Grosjean, A.S., Vennin, E., Olivier, N., Caravaca, G., Thomazo, C., Fara, E., Escarguel, G., Bylund, K.G., Jenks, J.F., Stephen, D.A., Brayard, A., 2018. Early Triassic environmental dynamics and microbial development during the Smithian–Spathian transition (Lower Weber Canyon, Utah, USA). Sediment. Geol. 363, 136–151. https://doi.org/10.1016/j.sedgeo.2017.11.009.

Guex, J., Hungerbühler, A., O'Dogherty, L., Atudorei, V., Taylor, D.G., Bucher, H., Bartolini, A., 2010. Spathian (Lower Triassic) ammonoids from western USA (Idaho, California, Utah and Nevada). Mém. Géol. (Lausanne) 49.

Guilbaud, R., Butler, I.B., Ellam, R.M., 2011. Abiotic Pyrite Formation Produces a Large Fe Isotope Fractionation. Science 1979 (332), 1548–1551. https://doi.org/10.1126/science.1202924.

Haq, B.U., Hardenbol, J., Vail, P.R., 1987. Chronology of Fluctuating Sea Levels since the Triassic. Science 1979 (235), 1156–1167. https://doi.org/10.1126/science.235.4793.1156.

Hautmann, M., Bucher, H., Brühwiler, T., Goudemand, N., Kaim, A., Nützel, A., 2011. An unusually diverse mollusc fauna from the earliest Triassic of South China and its implications for benthic recovery after the end-Permian biotic crisis. Geobios 44, 71–85. https://doi.org/10.1016/j.geobios.2010.07.004.

Heard, A.W., Dauphas, N., 2020. Constraints on the coevolution of oxic and sulfidic ocean iron sinks from archean-paleoproterozoic iron isotope records. Geology 48, 358–362. https://doi.org/10.1130/G46951.1.

Heydari, E., Moore, C.H., 1989. Burial Diagenesis and Thermochemical Sulfate Reduction, Smackover Formation, Southeastern Mississippi Salt Basin.

Ingersoll, R.V., 2008. Chapter 11 Subduction-Related Sedimentary Basins of the USA Cordillera, pp. 395–428. https://doi.org/10.1016/S1874-5997(08)00011-7.

Jattiot, R., Bucher, H., Brayard, A., Monnet, C., Jenks, J.F., Hautmann, M., 2016. Revision of the genus Anasibirites Mojsisovics (Ammonoidea): an iconic and cosmopolitan taxon of the late Smithian (Early Triassic) extinction. Pap. Palaeontol. 2, 155–188. https://doi.org/10.1002/spp2.1036.

Johnson, C.M., Beard, B.L., 2005. Biogeochemical cycling of iron isotopes. Science 1979. https://doi.org/10.1126/science.1112552.

Kaufman, A., Knoll, A., 1995. Neoproterozoic variations in the C-isotopic composition of seawater: stratigraphic and biogeochemical implications. Precambrian Res. 73, 27–49. https://doi.org/10.1016/0301-9268(94)00070-8.

Kidwell, S.M., Fursich, F.T., Aigner, T., 1986. Conceptual Framework for the Analysis and Classification of Fossil Concentrations. Palaios 1, 228. https://doi.org/10.2307/3514687.

Kirton, J.M.C., Woods, A.D., 2021. Stromatolites from the lower Triassic Virgin Limestone at Blue Diamond, NV USA: the role of dysoxia, enhanced calcification and nutrient availability in the growth of post-extinction microbialites. Glob. Planet. Chang. 198 https://doi.org/10.1016/j.gloplacha.2021.103429.

Klug, H.P., Alexander, L., 1974. X-Ray Diffraction Procedures for Polycrystalline and Amorphous Materials, First and Second ed. John Wiley and Sons, Inc, New York.

Kouketsu, Y., Nishiyama, T., Ikeda, T., Enami, M., 2014. Evaluation of residual pressure in an inclusion-host system using negative frequency shift of quartz Raman spectra. Am. Mineral. 99, 433–442. https://doi.org/10.2138/am.2014.4427.

Kühl, M., Jørgensen, B.B., 1992. Microsensor measurements of sulfate reduction and sulfide oxidation in compact microbial communities of aerobic biofilms. Appl. Environ. Microbiol. 58, 1164–1174. https://doi.org/10.1128/aem.58.4.1164-1174.1992.

Lin, Z., Sun, X., Lu, Y., Strauss, H., Xu, L., Gong, J., Teichert, B.M.A., Lu, R., Lu, H., Sun, W., Peckmann, J., 2017. The enrichment of heavy iron isotopes in authigenic pyrite as a possible indicator of sulfate-driven anaerobic oxidation of methane: Insights from the South China Sea. Chem. Geol. 449, 15–29. https://doi.org/10.1016/j.chemgeo.2016.11.032.

Liu, J., Pellerin, A., Izon, G., Wang, J., Antler, G., Liang, J., Su, P., Jørgensen, B.B., Ono, S., 2020. The multiple sulphur isotope fingerprint of a sub-seafloor oxidative sulphur cycle driven by iron. Earth Planet. Sci. Lett. 536 https://doi.org/10.1016/j.epsl.2020.116165.

Lucas, S.G., Krainer, K., Milner, A.R., 2007. The type section and age of the Timpoweap Member and stratigraphic nomenclature of the Triassic Moenkopi Group in Southwestern Utah. N. M. Mus. Nat. Hist. Sci. Bull. 40, 109–117.

Lyons, T.W., Anbar, A.D., Severmann, S., Scott, C., Gill, B.C., 2009. Tracking Euxinia in the Ancient Ocean: a multiproxy perspective and proterozoic case study. Annu. Rev. Earth Planet. Sci. 37, 507–534. https://doi.org/10.1146/annurev.earth.36.031207.124233.

Mansor, M., Fantle, M.S., 2019. A novel framework for interpreting pyrite-based Fe isotope records of the past. Geochim. Cosmochim. Acta 253, 39–62. https://doi.org/10.1016/j.gca.2019.03.017.

Marin-Carbonne, J., Rollion-Bard, C., Luais, B., 2011. In-situ measurements of iron isotopes by SIMS: MC-ICP-MS intercalibration and application to a magnetite crystal from the Gunflint chert. Chem. Geol. 285 (1–4), 50–61. https://doi.org/10.1016/j.chemgeo.2011.02.019.

Marin-Carbonne, J., Busigny, V., Miot, J., Rollion-Bard, C., Muller, E., Drabon, N., Jacob, D., Pont, S., Robyr, M., Bontognali, T.R.R., François, C., Reynaud, S., van Zuilen, M., Philippot, P., 2020. In Situ Fe and S isotope analyses in pyrite from the 3.2 Ga Mendon Formation (Barberton Greenstone Belt, South Africa): evidence for early microbial iron reduction. Geobiology 18, 306–325. https://doi.org/10.1111/gbi.12385.

Meister, P., Liu, B., Ferdelman, T.G., Jørgensen, B.B., Khalili, A., 2013. Control of sulphate and methane distributions in marine sediments by organic matter reactivity. Geochim. Cosmochim. Acta 104, 183–193. https://doi.org/10.1016/j.gca.2012.11.011.

Middelburg, J.J., 1989. A simple rate model for organic matter decomposition in marine sediments. Geochim. Cosmochim. Acta 53, 1577–1581. https://doi.org/10.1016/0016-7037(89)90239-1.

Olivier, N., Brayard, A., Fara, E., Bylund, K.G., Jenks, J.F., Vennin, E., Stephen, D.A., Escarguel, G., 2014. Smithian shoreline migrations and depositional settings in Timpoweap Canyon (Early Triassic, Utah, USA). Geol. Mag. 151, 938–955. https://doi.org/10.1017/S0016756813000988.

Olivier, N., Brayard, A., Vennin, E., Escarguel, G., Fara, E., Bylund, K.G., Jenks, J.F., Caravaca, G., Stephen, D.A., 2016. Evolution of depositional settings in the Torrey area during the Smithian (Early Triassic, Utah, USA) and their significance for the biotic recovery. Geol. J. 51, 600–626. https://doi.org/10.1002/gj.2663.

Olivier, N., Fara, E., Vennin, E., Bylund, K.G., Jenks, J.F., Escarguel, G., Stephen, D.A., Goudemand, N., Snyder, D., Thomazo, C., Brayard, A., 2018. Late Smithian microbial deposits and their lateral marine fossiliferous limestones (Early Triassic, Hurricane Cliffs, Utah, USA). Facies 64, 13. https://doi.org/10.1007/s10347-018-0526-3.

Orchard, M.J., 2007. Conodont diversity and evolution through the latest Permian and Early Triassic upheavals. Palaeogeogr. Palaeoclimatol. Palaeoecol. 252, 93–117. https://doi.org/10.1016/j.palaeo.2006.11.037.

Pasquier, V., Fike, D.A., Halevy, I., 2021. Sedimentary pyrite sulfur isotopes track the local dynamics of the Peruvian oxygen minimum zone. Nat. Commun. 12 https://doi.org/10.1038/s41467-021-24753-x.

Paull, R.A., Paull, R.K., 1993. Interpretation of Early Triassic nonmarine-marine relations, Utah, USA. In: Lucas, S.G., Morales, M. (Eds.), The Nonmarine Triassic, New Mexico Museum of Natural History and Science Bulletin, vol. 3, pp. 403–409.

Pruss, S., Fraiser, M., Bottjer, D.J., 2004. Proliferation of Early Triassic wrinkle structures: Implications for environmental stress following the end-Permian mass extinction. Geology 32, 461. https://doi.org/10.1130/G20354.1.

Rickard, D., 2019. Sedimentary pyrite framboid size-frequency distributions: a meta-analysis. Palaeogeogr. Palaeoclimatol. Palaeoecol. 522, 62–75. https://doi.org/10.1016/j.palaeo.2019.03.010.

Riedinger, N., Brunner, B., Krastel, S., Arnold, G.L., Wehrmann, L.M., Formolo, M.J., Beck, A., Bates, S.M., Henkel, S., Kasten, S., Lyons, T.W., 2017. Sulfur cycling in an iron oxide-dominated, dynamic marine depositional system: the argentine continental margin. Front. Earth Sci. (Lausanne) 5. https://doi.org/10.3389/feart.2017.00033.

Rouxel, O.J., Bekker, A., Edwards, K.J., 2005. Iron isotope constraints on the archean and paleoproterozoic ocean redox state. Science 1979 (307), 1088–1091. https://doi.org/10.1126/science.1105692.

Schubert, J.K., Bottjer, D.J., 1992. Early Triassic stromatolites as post-mass extinction disaster forms. Geology 20, 883. https://doi.org/10.1130/0091-7613(1992)020<0883:ETSAPM>2.3.CO;2.

Seilacher, A., Reif, W.-E., Westphal, F., Riding, R., Clarkson, E.N.K., Whittington, H.B., 1985. Sedimentological, ecological and temporal patterns of fossil Lagerstatten. Philos. Trans. R. Soc. Lond. B311, 5–23.

Severmann, S., Lyons, T.W., Anbar, A., McManus, J., Gordon, G., 2008. Modern iron isotope perspective on the benthic iron shuttle and the redox evolution of ancient oceans. Geology 36, 487–490. https://doi.org/10.1130/G24670A.1.

Shen, Y., Knoll, A.H., Walter, M.R., 2003. Evidence for low sulphate and anoxia in a mid-Proterozoic marine basin. Nature 423, 632–635. https://doi.org/10.1038/nature01651.

Shen, Y., Farquhar, J., Zhang, H., Masterson, A., Zhang, T., Wing, B.A., 2011. Multiple S-isotopic evidence for episodic shoaling of anoxic water during late Permian mass extinction. Nat. Commun. 2, 210. https://doi.org/10.1038/ncomms1217.

Smith, C.P.A., Laville, T., Fara, E., Escarguel, G., Olivier, N., Vennin, E., Goudemand, N., Bylund, K.G., Jenks, J.F., Stephen, D.A., Hautmann, M., Charbonnier, S., Krumenacker, L.J., Brayard, A., 2021. Exceptional fossil assemblages confirm the existence of complex Early Triassic ecosystems during the early Spathian. Sci. Rep. 11 https://doi.org/10.1038/s41598-021-99056-8.

Song, H., Wignall, P.B., Tong, J., Yin, H., 2013. Two pulses of extinction during the Permian-Triassic crisis. Nat. Geosci. 6, 52–56. https://doi.org/10.1038/ngeo1649.

Song, H., Du, Y., Algeo, T.J., Tong, J., Owens, J.D., Song, Haijun, Tian, L., Qiu, H., Zhu, Y., Lyons, T.W., 2019. Cooling-driven oceanic anoxia across the Smithian/Spathian boundary (mid-Early Triassic). Earth Sci. Rev. https://doi.org/10.1016/j.earscirev.2019.01.009.

Sun, Y.D., Wignall, P.B., Joachimski, M.M., Bond, D.P.G., Grasby, S.E., Sun, S., Yan, C.B., Wang, L.N., Chen, Y.L., Lai, X.L., 2015. High amplitude redox changes in the late Early Triassic of South China and the Smithian–Spathian extinction. Palaeogeogr. Palaeoclimatol. Palaeoecol. 427, 62–78. https://doi.org/10.1016/j.palaeo.2015.03.038.

Swart, P.K., 2015. The geochemistry of carbonate diagenesis: the past, present and future. Sedimentology 62 (5), 1233–1304. https://doi.org/10.1111/sed.12205.

Thomazo, C., Brayard, A., Elmeknassi, S., Vennin, E., Olivier, N., Caravaca, G., Escarguel, G., Fara, E., Bylund, K.G., Jenks, J.F., Stephen, D.A., Killingsworth, B.,

Sansjofre, P., Cartigny, P., 2019. Multiple sulfur isotope signals associated with the late Smithian event and the Smithian/Spathian boundary. Earth Sci. Rev. https://doi.org/10.1016/j.earscirev.2018.06.019.

Vennin, E., Olivier, N., Brayard, A., Bour, I., Thomazo, C., Escarguel, G., Fara, E., Bylund, K.G., Jenks, J.F., Stephen, D.A., Hofmann, R., 2015. Microbial deposits in the aftermath of the end-Permian mass extinction: a diverging case from the Mineral Mountains (Utah, USA). Sedimentology 62, 753–792. https://doi.org/10.1111/sed.12166.

Virtasalo, J.J., Whitehouse, M.J., Kotilainen, A.T., 2013. Iron isotope heterogeneity in pyrite fillings of Holocene worm burrows. Geology 41, 39–42. https://doi.org/10.1130/G33556.1.

Welch, S.A., Beard, B.L., Johnson, C.M., Braterman, P.S., 2003. Kinetic and equilibrium Fe isotope fractionation between aqueous Fe(II) and Fe(III). Geochimica et Cosmochimica Acta 67, 4231–4250. https://doi.org/10.1016/S0016-7037(03)00266-7.

Wilkin, R.T., Barnes, H.L., 1997. Pyrite formation in an anoxic estuarine basin. Am. J. Sci. 297, 620–650. https://doi.org/10.2475/ajs.297.6.620.

Wilkin, R.T., Barnes, H.L., Brantley, S.L., 1996. The size distribution of framboidal pyrite in modern sediments: an indicator of redox conditions. Geochim. Cosmochim. Acta 60, 3897–3912. https://doi.org/10.1016/0016-7037(96)00209-8.

Woods, A.D., 2014. Assessing Early Triassic paleoceanographic conditions via unusual sedimentary fabrics and features. Earth Sci. Rev. 137, 6–18. https://doi.org/10.1016/j.earscirev.2013.08.015.

Wu, L., Beard, B.L., Roden, E.E., Johnson, C.M., 2011. Stable iron isotope fractionation between aqueous Fe(II) and hydrous ferric oxide. Environ. Sci. Technol. 45, 1847–1852. https://doi.org/10.1021/es103171x.

Zhang, G., Zhang, X., Li, D., Farquhar, J., Shen, S., Chen, X., Shen, Y., 2015. Widespread shoaling of sulfidic waters linked to the end-Guadalupian (Permian) mass extinction. Geology 43, 1091–1094. https://doi.org/10.1130/G37284.1.

Zhang, L., Orchard, M.J., Brayard, A., Algeo, T.J., Zhao, L., Chen, Z.Q., Lyu, Z., 2019. The Smithian/Spathian boundary (late Early Triassic): a review of ammonoid, conodont, and carbon-isotopic criteria. Earth Sci. Rev. https://doi.org/10.1016/j.earscirev.2019.02.014.

Zhao, H., Dahl, T.W., Chen, Z.Q., Algeo, T.J., Zhang, L., Liu, Y., Hu, Zhaochu, Hu, Zihao, 2020. Anomalous marine calcium cycle linked to carbonate factory change after the Smithian thermal Maximum (Early Triassic). Earth Sci. Rev. https://doi.org/10.1016/j.earscirev.2020.103418.